Research article

Automated riverbed composition analysis using Deep Learning on underwater images

Alexander A. Ermilov[1], Gergely Benkő[1] and Sándor Baranya[1]

[1]Department of Hydraulic and Water Resources Engineering, Budapest University of Technology and Economics, Budapest, 1111, Hungary

Correspondence to: Alexander A. Ermilov (ermilov.alexander@emk.bme.hu)

Abstract. The sediment of alluvial riverbeds plays a significant role in river systems both in engineering and natural processes. However, the sediment composition can show high spatial and temporal heterogeneity, even on river reach scale, making it difficult to representatively sample and assess. Conventional sampling methods are inadequate and time-consuming for effectively capturing the variability of bed surface texture in these situations. In this study, we overcome this issue by adopting an image-based, Deep Learning (DL) algorithm. The algorithm was trained to recognise main sediment classes in videos that were taken along cross-sections underwater in the Danube river. 27 river bed samples were collected and analyzed for validation.. The introduced DL-based method is fast, i.e., the videos of 300-400-meter-long sections can be analysed within minutes, with continuous spatial sampling distribution (i.e., the whole riverbed along the path is mapped with images, in cca. $0.3 - 1$ m² sized, overlapping windows). The quality of the trained algorithm was evaluated i) mathematically by dividing the annotated images into test and validation sets, and also via ii) intercomparison with other direct (sieving of physical samples) and indirect sampling methods (wavelet-based image processing of the riverbed images), focusing on the percentages of the detected sediment fractions. For the final evaluation, the sieving analysis of the collected physical samples were considered as the ground truth. After correcting for samples affected by bed armouring, comparison of the DL approach with 14 physical samples yielded a mean classification error of 4.5%.Besides, the spatial trend in the fraction changes was also well captured along the cross-sections, based upon the visual evaluation of the footages. Suggestions for performing proper field measurements are also given, furthermore, possibilities for combining the algorithm with other techniques are highlighted, briefly showcasing the multi-purpose of underwater videos for hydromorphological assessment.

Keywords: riverbed texture, underwater mapping, sediment classes, Artificial Intelligence, Deep Learning, image-based

1 Introduction

The physical composition of a riverbed plays a crucial role in fluvial hydromorphological processes, as a sort of boundary condition in the interaction mechanisms between the flow and the solid bed. Within these processes, the grains on the riverbed are responsible for multiple phenomena, such as flow resistance (Vanoni and Hwang, 1967; Zhou et al., 2021), stability of the riverbed (Staudt et al., 2018; Obodovskyi et al., 2020), development of bed armour (Rákóczi, 1987; Ferdowsi et al., 2017), sediment clogging (Rákóczi, 1997; Fetzer et al., 2017), fish shelter (Scheder et al., 2015), etc. Through these physical processes, the bed material composition has a determining effect on numerous river-uses, e.g., possibilities of inland waterway transport (Xiao et al., 2021), drinking water supply through bank filtration (Cui et al., 2021), or the quality of riverine habitats (Muñoz-Mas et al., 2019)..

Knowledge of riverbed morphology and sediment composition (sand, gravel and cobble content) is therefore of major importance in river hydromorphology. In order to gain information about riverbed sediments, in situ field sampling methodologies are implemented.

Traditionally, bed material sampling methods are intrusive (i.e., sediment is physically extracted from the bed for follow-up analysis) and carried out via collecting the sediment grains one-by-one (areal, grid-by-number and pebble count methods, see e.g., Bunte and Abt, 2001; Guerit et al., 2018) or in a larger amount by a variety of grab samplers (volumetric methods, such as WMO, 1981; Singer, 2008). This is then followed by measuring their sizes individually on-site or transporting them to a laboratory for mass-sieving analysis (Fehr, 1987; Diplas, 1988; Bunte and Abt, 2001). These sampling procedures are time- and energy consuming, especially in large gravel and mixed bed rivers, where characteristic grain sizes can strongly vary both in time and space (Wolcott and Church, 1991; USDA, 2007), requiring a dense sampling point allocation. The same goes for critical river reaches, where significant human impact led to severe changes in the morphological state of the rivers (e.g., the Upper section of the Hungarian Danube; Török and Baranya, 2017). When assessing bed material composition on a river reach scale, experts usually try to extrapolate from the samples, and describe larger regions of the bed (even several thousand m^2) by data gathered in a few, several dozen points (see e.g., USDA, 2007; Haddadchi et al., 2018; Baranya et al., 2018; Sun et al., 2021). Gaining a representative amount of the sediment samples is also a critical issue. For instance, following statistical criteria such as those of Kellerhals and Bray (1971) or Adams (1979), a representative sample should weigh ten-to-hundred kg. Additionally, physical bed material sampling methods are unable to directly quantify important, hydromorphological features such as roughness or bedforms (Graham et al., 2005). Due to these constraints, surrogate approaches have recently been tested to analyse the riverbed. Examples are introduced in the rest of this section. Unlike the conventional methods, these techniques are non-intrusive and rely on computers and other instrumentation to decrease the need of human intervention and speed up the analyses.

One group of the surrogate approaches is the acoustic methods, where an acoustic wave source (e.g., an Acoustic Doppler Current Profiler; ADCP) is pointed towards the riverbed from a moving vessel, emitting a signal. The strength and frequency of this signal is measured while it passes through the water column, reflecting back to the receiver from the sediment transported by the river, and finally from the riverbed itself. This approach is fast and larger areas can be covered relatively quickly (Grams et al., 2013). While it has already become widely used for describing sediment movement (i.e., suspended sediment, Guerrero et al., 2016; bedload, Muste et al., 2016; and indirectly flow velocity; Shields and Rigby, 2005) and channel shape (Zhang et al., 2008), it has not reached similar breakthrough for riverbed material analysis. Researchers experimented with the reflecting signal strength [dB] from the riverbed (e.g., Shields, 2010) to establish its relationship with the riverbed material. Their hypothesis was that the absorption (and hence the reflectance) of the acoustic waves reaching the bed correlates with the type of bed sediment. Following initial successes, the method presented several disadvantages and limitations, hence it could not establish itself as surrogate method for riverbed material measurements so far. For example, Shields (2010) showed that it was necessary to apply instrument specific coefficients to convert the signal strength into bed hardness, and these coefficients could only be derived by first validating each instrument using collected sediment samples with corresponding ADCP data. Moreover, the method was sensitive to the bulk density of the sediment and to bedforms. Based on his results and observations, the sediment classification could only extend to

differentiate between cohesive (clay, silt) and non-cohesive (sand, gravel) sediment patches, but gravel could not be distinguished strongly from sand as they produced similar backscatter strengths. Buscombe et al. (2014a; 2014b) further elaborated on the topic and successfully developed a better, less limited, decision tree-based approach. They showed that spectral analysis of the backscatter is much more effective for differentiating the sediment types compared to the statistical analysis used by Shields. With this approach it became possible to classify homogenous sand, gravel, and cobble patches. However, Buscombe et al. (2014a, 2014b) also emphasizes that acoustic approaches are not capable of separating the effects of surface roughness from the effects of bedforms, therefore the selection of an appropriate ensemble averaging window size is of great importance for their introduced method. This size has to be small enough to not include morphological signal, for which however, the a priori analyses of riverbed elevation profiles is needed at each site. Furthermore, they suggest their method is sensitive to and limited by high concentrations of (especially cohesive) sediment, therefore its application to heterogeneous riverbeds would require site specific calibrations. The above-mentioned studies also note that acoustic methods in general inherently do not allow the measurement of individual sediment grains due to their spatial averaging nature. The detected signal strength correlates with the median grainsize of the covered area, information about other nominal grainsizes cannot be gained.

Another group of the surrogate approaches is the application of photography (Adams, 1979; Ibbekken and Schleyer, 1986) and later computer vision or image-processing techniques. During the last two decades, two major subgroups emerged: one uses object- and edge detection (by finding abrupt changes in intensity and brightness of the image, segmenting objects from each other; Sime and Ferguson, 2003; Detert and Weitbrecht, 2013), and the other one analyses the textural properties of the whole image, using autocorrelation and semi-variance methods to define empirical relationship between image texture and the grain sizes of the photographed sediments (Rubin, 2004; Verdú et al., 2005). Both image processing approaches were very time consuming and required mostly site-specific manual settings, however, a few transferable and more automated techniques have also been developed recently (e.g., Graham et al., 2005; Buscombe, 2013). Even though there is a continuous improvement in the applied image-based bed sediment analysis methods, there are still major limitations the users face with, such as:

- Most of the studies (all the ones listed above) focuses on gravel bed rivers, and only a few exceptions can be found in the literature where sand is also accounted for (texture-based methods;e.g.: Buscombe, 2013).
- The adaptation environment was typically non-submerged sediment, instead of underwater conditions (a few exceptions: Chezar and Rubin, 2004; Warrick et al., 2009).
- The computational demand of the image processing is high (e.g., one to ten minutes per image; Detert and Weitbrecht, 2013).
- The analysis requires operator expertise (higher than in case of any conventional method).
- There is an inherent pixel- and image resolution limit (Buscombe and Masselink, 2008 Cheng, 2015; Purinton and Bookhagen, 2019). The finer the sediment, the higher resolution of the images is required (higher calculation time), or they must be taken from a closer position (smaller area and sample per image).

Nowadays, with the rising popularity of Artificial Intelligence (AI), several Machine Learning (ML) techniques have been implemented in image recognition as well. The main approaches of segmentation contra textural analysis still remain; however, an AI defines the empirical relationship between the object sizes (Igathinatane et al., 2009; Kim et al., 2020) or texture types (Buscombe and Ritchie, 2018) in the images and their real sizes. In the field of river sedimentology a few examples can already be found, where ML (e.g., Deep Learning; DL) was implemented. For instance, Rozniak et al. (2019) developed an algorithm for gravel-bed rivers, performing textural analysis. With this approach, information is not gained on individual grains (e.g., their individual shape and position), but rather the general grain size distribution (GSD) of the whole images. At certain points of the studied river basins, conventional physical samplings (pebble count) were performed to provide real GSD information. Using this data, the algorithm was trained (with ~1000 images) to estimate GSD for the rest of the study site, based on the images. The method worked for areas where grain diameters were larger than 5 mm, and the sediment was well-sorted. The developed method showed sensitivity to sand coverage, blurs, reduced illuminations (e.g., shadows) and white pixels. Soloy et al. (2020) presented an algorithm which used object detection on gravel- and cobble covered beaches to calculate individual grain sizes and shapes. 46 images were used for the model training, however, the number of images were multiplied with data augmentation (rotating, cropping, blurring the images; see Perez and Wang, 2017) to enhance the learning session and increase the input data. The method was able to reach a limited execution speed of a few seconds per m^2 and adequately measured the sizes of gravels. Ren et al. (2020) applied an ensemble bagging-based Machine Learning (ML) algorithm to estimate GSD along the 70 km long Hanford Reach of the Columbia River. Due to its economic importance, a large amount of measurement data has been accumulated for this study site over the years, making it ideal for using ML. By the time of the study, 13,372 scaled images (i.e., their millimetre/pixel ratio was known) were taken both underwater and in the dry zones, covering approx. 1 m^2 area each. The distance between the image-sampling points was generally between 50-70 m. An expert defined the GSD (8 sediment classes) of each image by using a special, visual evaluation-classification methodology (Delong and Brusven, 1991; Geist et al., 2000). This dataset was fed to a ML algorithm along with their corresponding bathymetric attributes and hydrodynamic properties, simulated with a 2D hydrodynamic model. Then, it was tested to predict the sediment classes based on the hydrodynamic parameters only. The algorithm performed with a mean accuracy of 53%. Even though this method was not image-based (only indirectly, via the origin of the GSD data), it highlighted the possibilities of an AI for a predictive model, using a high-dimensional dataset. Having such a large data of grain size information can be considered exceptional and takes a huge amount of time to gather, even with the visual classification approach they adapted. Moreover, this was still considered spatially sparse information (point-like measurements, 1 m^2 covered area/image dozens of meters away from each other). Buscombe (2020) used a set of 400 scaled images to train an AI algorithm on image texture properties, using another image-processing method (Barnard et al., 2007) for validation. The algorithm reached a good result for not only gravel, but sand GSD calculation as well, outperforming an earlier, but promising, texture-based method (wavelet analysis; Buscombe, 2013). In addition, the method required fewer calibration parameters than the wavelet image-processing approach. The study also foresaw the possibility to train an AI which estimates the real sizes of the grains, without knowing the scale of one pixel (mm/pixel ratio) if the training is done properly. The AI might learn unknown relationships between the texture and sizes if it is provided with a wide variety (images of several sediment classes) and scale (mm/pixel ratio)) of dataset (however, it is also prone to learn unwanted biases). Recently, Takechi et al. (2021) further

elaborated on the importance of shadow- detection and removal, using a dataset of 500 pictures for training a texture-based AI, with the help of an object-detecting image-processing technique (Basegrain; Detert and Weitbrecht, 2013). The previously presented studies, applying ML and DL techniques, significantly contributed to the development and improvement of surrogate sampling methods, incorporating the great potential in AI. However, there are still several shortcomings to these procedures. Firstly, none of the image-based AI studies used underwater recordings, even though the underwater environment offers completely different challenges. Secondly, the training images were always scaled, i.e., the sizes of the grains could be easily reconstructed, which is again complicated to accomplish in a river. Lastly, they were not adapted for continuous (i.e., spatially dense) measurement, but rather focused on a sparse grid-like approach.

The goal of this study is to further investigate the applicability of image processing as a surrogate method, and attempt solve the shortcomings of previous AI-based approaches. Hence, we introduce a riverbed material analysing, DL algorithm and field measurement methodology, along with our first set of results. The introduced technique can be used to measure the gravel and sand content of the submerged riverbed surface. It aims to eventually become a practical tool for exploratory mapping, by detecting sedimentation features (e.g., deposition zones of fine sediment, colmation zones, bed armour) and helping decision making for river sedimentation management. Also, the long-term hypothesis of the authors includes the creation of an image-based measurement methodology, where underwater videos of the riverbed could serve multiple sediment related purposes simultaneously. Part of which is the current approach for mapping the riverbed material texture and composition. Others include measuring the surface roughness of the bed (Ermilov et al., 2020) and detecting bedload movement (Ermilov et al., 2022).

Compared to the studies introduced earlier, the main novelty of our study is that both the training and analysed videos are recorded underwater, continuously along cross-sections of a large river. Furthermore, the training is unscaled, i.e., the camera-riverbed distance varies while recording the videos, without considering image-scale. Moreover, compared to the relatively low number of training images in most previous studies, we used a very large dataset (~15000) of sediment images for the texture-based AI, containing mostly sand, gravel, cobble, and to a smaller extent: bedrock together with some other, non-sediment related objects.

2 Methods

2.1 Case studies

The results presented in this study are based on riverbed videos taken during three measurement campaigns, in sections of the Danube River, Hungary. The first campaign was at Site A, Ercsi settlement (~ 1606 rkm) where 3 transects were recorded, the second one was at Site B, Gönyű settlement (~ 1791 rkm) with 2 transects, and the third was at Site C, near to Göd settlement (~ 1667 rkm) with 2 transects (Fig. 1). Each transect was recorded separately (one video per transect), therefore our dataset included a total of 8 videos.

194
195 **Figure 1: The location of the riverbed videos, where the underwater recordings took place. All sites were located in**
196 **Hungary, Central Europe. The surveys were carried out on the Danube River, Hungary's largest river.**

197   The training of the DL algorithm was done using the video images of Site C and a portion of A (test set; see later

198   in Section 2.3), while Site B and the rest of the images from A served for validation. The measurements were

199   carried out during daytime, at mid-water regime (Q = 1900 m^3/s) in case of Site A, and low water regime (Q =

200   1350 m^3/s) at Site B, and Site C (Q = 700 m^3/s). This latter site served only for increasing the training image

201   dataset (i.e., conventional samplings were not carried out at the time of recording the videos), thus we do not go

202   into further details with it for the rest of the study, but the main characteristics are listed in Table 1.

203

	Site A	Site B	Site C
Q_{survey} [m³/s]	1900	1350	700
B_{survey} [m]	300 – 450		
$H_{mean, survey}$ [m]	3.5 - 4.5		
S_{survey} [cm/km]	15		
SSC_{survey} [mg/l]	25	20	14
Characteristic riverbed sediment	gravel, sandy gravel	gravel, gravelly sand	gravel, sandy gravel
$Q_{annual,mean}$ [m³/s]	2000	2200	1400
$Q_{1\%}$ [m³/s]	5300	5500	4700

Table 1: Main hydromorphological parameters of the measurement sites. Q_{survey}: discharge during survey; B_{survey}: river width during survey; $H_{mean,survey}$: mean water depth during the survey; S_{survey}: riverbed slope during survey; SSC_{survey}: mean suspended sediment concentration during the survey; $Q_{annual, mean.}$: annual-mean of the discharge at the site; $Q_{1\%}$: flood with 1% annual exceedance probability.

As underwater visibility conditions are influenced by the suspended sediment (SSC_{survey} – susp. sed. concentration), the characteristics of this sediment transport is also included in Table 1. The highest water depths were around 6-7 m in all cases. In Site A, measurements included mapping of the riverbed with a camera along three separate transects (Fig. 2a). At Site B, two transects were recorded (Fig. 2b).

212
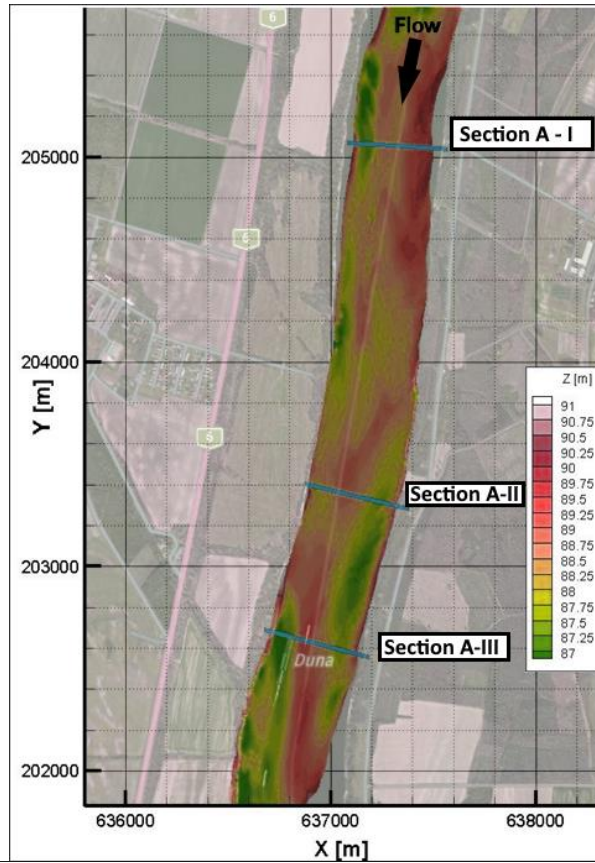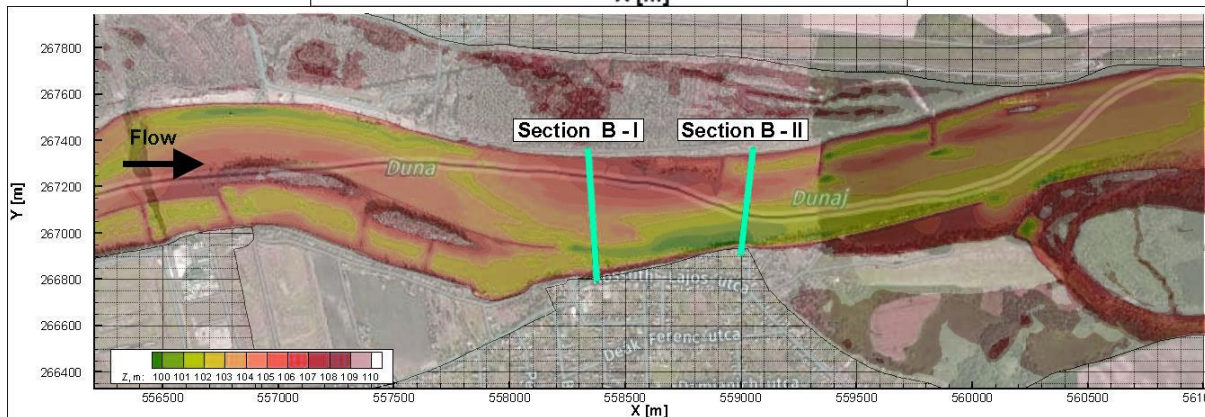
213
214 **Figure 2: Bathymetry of Site A and B The measurement cross-sections are also marked. The vessel moved along these**
215 **lines from one bank to the other, while carrying out ADCP measurement and recording riverbed videos. Physical bed**
216 **material samples were also collected in certain points of these sections. The X and Y coordinates are given in EOV,**
217 **which refers to the Hungarian Uniform National Projection system,**

218

219 **2.2 Field data collection**

220 Fig. 3 presents a sketch of the measurement process with the equipment and a close-up of the underwater
221 instrumentation. During the field measurements, the camera was attached to a streamlined weight (originally used
222 as an isokinetic suspended sediment sampler) and lowered into the water from the vessel by an electric reel. The
223 camera was positioned perpendicularly to the water and the riverbed, in front of the nose of the weight. Next to
224 the camera, two diving lights worked as underwater light sources, focusing into the camera's field of view (FoV).
225 In addition, four laser pointers were also equipped in hand-made isolation cases to provide possible scales for
226 secondary measurements. They were also perpendicular to the bottom, projecting their points onto the underwater

camera field of view. Their purpose was to ensure a visible scale (mm/pixel ratio) in the video footages for validation. During the measurement procedure, a vessel crossed the river slowly through river transects, while the position of the above detailed equipment was constantly adjusted by the reel. Simultaneously, ADCP and RTK GPS measurement were carried out by the same vessel, providing water depth, riverbed geometry, flow velocity, ship velocity and position data. Based on this information and by constantly checking the camera's live footage on deck, the camera was lowered or lifted to keep the bed in camera sight and avoid colliding with it. The sufficient camera – riverbed distance depended on the suspended sediment concentration near the bed and the used illumination. The reel was equipped with a register, with its zero adjusted to the water surface. This register was showing the length of cable already released under the water, effectively the rough distance between the water surface and the camera (i.e., the end of the cable).Due to the drag force this distance was not vertical, but this value was continuously compared to the water depth measured by the ADCP. Differencing these two values, an approximation for the camera – riverbed distance was given all time. The sufficient difference could be established by monitoring the camera footage while lowering the device towards the bed. This value was then to be maintained with smaller corrections during the survey of the given cross-section, always supported by observing the camera recording, and adjusting to environmental changes. The vessel's speed was also adjusted based on the video and slowed down if the video was blurry or the camera got too far away from the bed (see later in Section 3.3). The measurements required three personnel to i) drive the vessel, ii) handle the reel, adjust the equipment position, and monitor the camera footage, iii) monitor the ADCP data, while communicating with the other personnel (see Fig. 3).
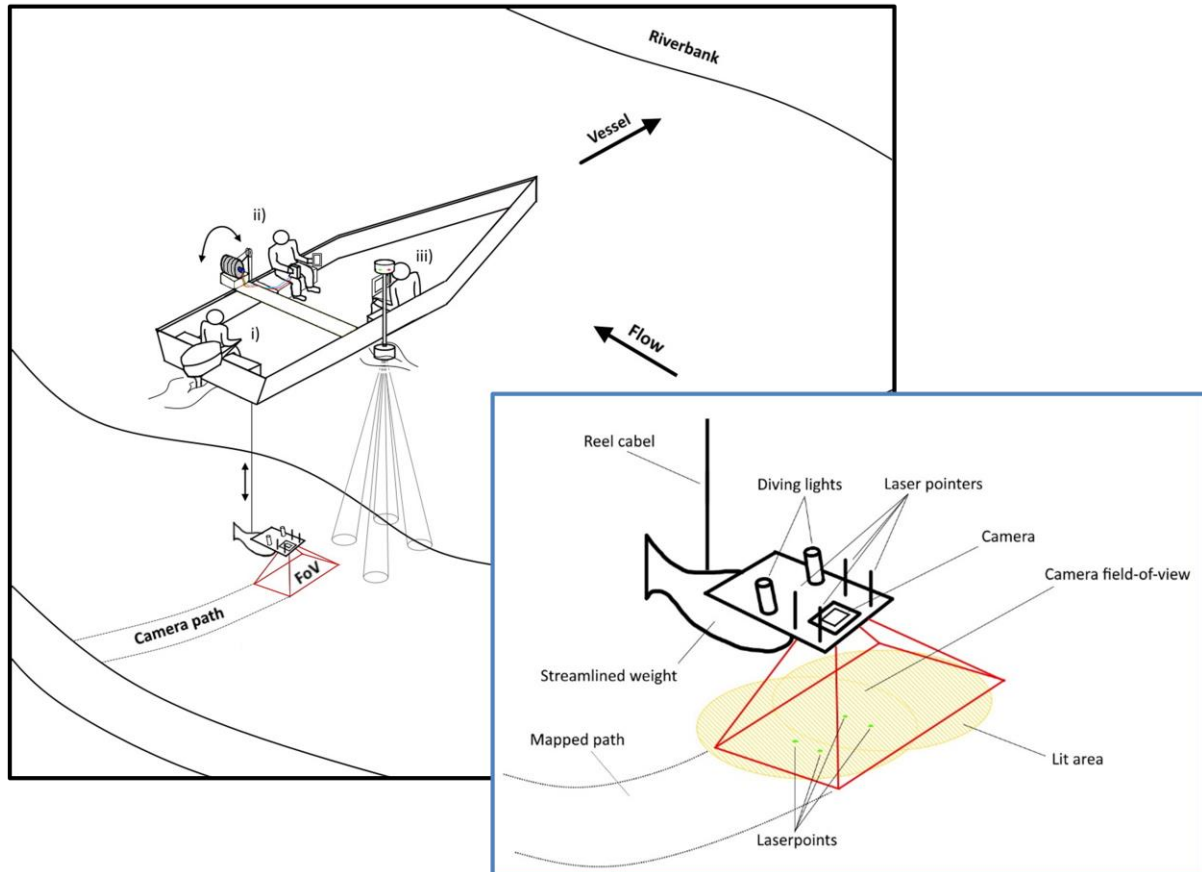
246
247 **Figure 3: Left: sketch of the measurement process. The vessel was moving perpendicular to the riverbank along a cross-**
248 **section (i). A reel was used to lower a camera close to the riverbed (ii). Simultaneously, the bed topography and water**
249 **depth were measured by an ADCP (iii). Right: Close-up sketch of the underwater instrumentation.**

250 The video recordings were made with a GOPRO Hero 7 and a Hero 4 commercial action cameras. Image
251 resolutions were set to 2704x2028 (2.7K) with 60 frame per second (fps) and 1920x1080 (1080p) with 48 fps,
252 respectively. Other parameters were left at their default (see GOPRO 2014; 2018), resulting in slightly different
253 quality of produced images between the two cameras. We found that a 0.2-0.45 m/s vessel speed with 60 fps
254 recording frequency was ideal to retrieve satisfactory images in a range of 0.4-1.6 m camera-bed distances. This
255 meant approximately 15 minutes long measurements per transects. Further attention needed to be paid to the reel
256 and its cable during the crossing when the equipment was on the upstream side of the boat. If the flow velocities
257 are relatively high (compared to the total submerged weight of the underwater equipment), the cable can be pressed
258 against the vessel-body due to the force from the flow itself, causing the reel cable to jump to the side and leave
259 its guide. This results in the equipment falling to the riverbed and the measurement must be stopped to reinstall
260 the cable. For illumination, a diving light with 1500 lumen brightness and 75° beam divergence, and one with
261 1800 lumen and 8° were used. The four lasers for scaling had 450-520 nm (purple and green) wavelength and 1-
262 5 mW nominal power. Power supply was ensured with batteries for all instruments.

263
264 At Site A and Site B, conventional bed material (physical) samplings were also carried out by a grabbing (bucket)
265 sampler along the analysed transects. At each cross-section 4-5 samples were taken, with one exception where we
266 had 10. The measured GSDs were used to validate results of the AI algorithm. Separately, a visual evaluation of
267 the videos was also carried out, where a person divided the transects into subsections based on their dominant
268 sediment classes, after watching the footages.

2.3 Image analysis: Artificial Intelligence and the wavelet method

In this study, we built on the former experiences of the authors, using Benkő et al., 2020 as a proof-of-concept, where the developed algorithm was applied for analysing drone videos of a dry riverbed. The same architecture was used in this study, which is based on the widely used Google's DeeplabV3+ Mobilnet, in which many novel and state-of-the-art solutions are implemented (e.g., Atrous Spatial Pyramid Pooling; Chen et al., 2018). The model was implemented with Pytorch, exploiting its handy API and backward compatibility. The main goal was to build a deep neural network model which can recognise and categorise (via semantic segmentation; Chen et al., 2018) at least three main sediment size classes, i.e., sand, gravel and cobble, in the images, while being quickly deployable. The benefit of the introduced method compared to conventional imagery methods lies in the potential of automation and increased speed. If the annotation and training is carried out thoroughly, analysing further videos can run effortlessly, while the computation time can be scaled down either vertically (using stronger GPUs) or horizontally (increasing the number of GPUs; if parallel analysis of images is desired). In this study a TESLA K80 24GB GDDR5 348bit GPU, an Intel Skylake Intel® Xeon® Gold 6144 Processor (24.75M Cache, 3.50 GHz) CPU with 13GB RAM was used. Also, contrary to other novel image-processing approaches in riverine sediment research (Buscombe, 2013; Detert and Weitbrecht, 2013), the deep convolutional neural network is much less limited by image resolution and mm/pixel ratios, because it does not rely on precise pixel count. This is an important advantage to be exploited here, as we perform non-scaled training and measurements with the DL, i.e., camera-bed distance constantly changed, and size-reference was not used in the images by the DL.

Fig. 4 presents the flowchart of our DL-based image processing methodology. The first step after capturing the videos was to cut them into frames, during which the videos were exploded into sequential images. Our measurement setup proved to be slightly nose-heavy. Due to this, and the drag force combined, the camera tilted forward during the measurements. As a result, the lower parts of the raw images were sometimes too dark, as the camera was looking over the riverbed, and not at the lit part of the bed. In this study, this problem was handled by simply cutting out the lower 25% of the images as this was the region usually containing the dark, unlit areas. Brightening and sharpening filters were applied on the remaining part of the images to improve their quality. Next, the ones with clearest outlines and best visibility were chosen. This selection process was necessary because this way the delineation process (learning the prominent characteristics of each class) can be executed accurately, without the presence of misleading or confusing images, e.g., blurry or dark pictures where the features are hard to recognise. For training purposes, we chose three videos from different sections each being ~15 minutes long with 60 fps and 48 fps, resulting in 129 600 frames. In fact, such a large dataset was not needed due to the strong similarity of the consecutive frames. The number of images to be annotated and augmented were therefore

Data creation

- Using underwater videos
- Large number of images
- Not fixed elevation from riverbed
- With multiple frame rate
- Selecting images according to variance and visibility

White Balance Upgrade

- Balance correction on images with low visibility
- Histogram equalisation with Simple Colour Balance for enhancing edges

Data annotation

- Separating 10 different classes in the images: silt-clay, sand, gravel, cobble, boulder, bedrock, clam-upside, clam-downside, vegetation, unidentified

Data augmentation

- Increasing data size by: mirroring cropping, rotating, darkening, sharpening, bluring, white- and colour balancing images

Training

- On powerful virtual machines with Tesla K80 GPUs
- 80/20 training/test split
- 14784 images were used. 11827 for training and 2957 for validation

Visualization and analysis

- Overall pixel accuracy: 96.35% (mean percent of pixels classified correctly per image during validation)
- Mean IoU: 41.46%
- Overlaying image masks prepared to show the precision of the method
- Comparing DL results on new data with other sampling methods

540

Figure 4: Flowchart of the applied methodology.

decreased to ~2000. We also performed a white balance correction on some of the images to improve visibility, making it even easier to later define the sediment class boundaries. We used an additional algorithm to generate more data, with the so-called Simplest Colour Balance method (Limare et al., 2011). It is a simple, but powerful histogram equalisation algorithm which helps to equalise the roughness in pixel distribution.

These steps were followed by the annotation, where we distinguished ten classes: silt-clay, sand, gravel, cobble, boulder (mainly ripraps), bedrock, clam-upside, clam-downside, vegetation, unidentified (e.g., wreckages). Annotation was carried out by a trained personnel, not by the authors, and performed with the help of an open-source software called PixelAnnotationTool (Breheret, 2017), which enables the user to colour mask large parts of an image based on colour change derivatives (i.e., colour masking part of the images which belong to the same class, e.g., purple/red – sand, green – gravel, yellow – cobble, etc.). The masks and outlines were drawn manually, together with the so-called watershed annotation. That is, when a line was drawn, the algorithm checked for similar pixels in the vicinity and automatically annotated them with the same class. The annotation was followed by a data augmentation step where beside mirroring, cropping, rotating the images (to decrease the chance of overfitting), we also convolved them with different filters. These filters added normally distributed noise to the photos to influence the watershed algorithm and applied sharpening, blurring, darkening, and white balance enhancement. Thus, at the data level, we tried to ensure that any changes in water purity, light, and transparency, as well as colour changes, were adequately represented during training. Images were uniformly converted to 960x540 resolution, scaling them down to make them more usable to fit in the GPU's memory. The next step was to convert all the images from RGB (Red-Green-Blue) based colour to grayscale. This is important because colour images have 3-channels, so that they contain a red, a green, and a blue layer, while grayscale images' pixel can only take one value between 0 and 255. With this colour conversion we obtained a threefold increase in computational speed. In total, a dataset of 14,784 human-annotated images was prepared (from the ~2000 images of the 3 training videos). The next step was to separate this dataset into training and validation sets. In this study, we used 80% of it for training the DL algorithm, while 20% was withhold and reserved for the validation of the training. It was important to mix the images so that the algorithm selects batches in a pseudorandom manner during training, thus preventing the model from being overfitted. Finally, after

several changes in the hyperparameters (i.e., tuning), the evaluation and visualisation of the training results were performed. Tuning is a general task to do when building DL Networks, as these hyperparameters determine the structure of the network and the training process itself. Learning rate, for example, describes how fast the network refreshes, updates itself during the training. If this parameter is set too high, the training process finishes quickly, but convergence may not be reached. If it is too low, the process is going to be slow, but it converges. For this reason, nowadays the learning rate decay technique is used, where one starts out with a large learning rate, then slowly reduces it. The technique generally improves optimization and generalization of the DL Networks (You et al., 2019). In our case, learning rate was initialised to 0.01, with 30000 iteration steps, and the learning rate was reset after every 5000 iterations with a decay of 0.1. Another important parameter was the batch size, which sets the number of samples fed to the network before it updates itself. Theoretical and empirical evidence suggest that learning rate and batch size are highly important for the generalization ability of a network (He et al., 2019). In our study, a batch size of 16 was used (other general values in the literature are 32, 64, 128, 256). We used a cross-entropy loss function.

As previously discussed, the training of the deep learning (DL) algorithm proceeded without the application of scaling, obviating the need for the laser equipment. Nevertheless, our original intention was to employ laser pointers to establish a spatial scale for the recorded videos, serving as a supplementary validation measure. Regrettably, the lasers did not operate as initially anticipated, rendering their continuous utilization during the cross-sectional surveys and the pursuit of transactional scaling and validation unfeasible. Consequently, we shifted our focus to validation at specific physical sampling points, where we could utilize the lasers properly. We adopted a textural image-processing approach to analyse the video images captured at these sampling locations. In this regard, we opted for the previously mentioned, transferable wavelet-based signal- and image-processing technique. This method allows for the computation of the image-based grain size distribution from the selected images. The analysis entails examining the grey-scale intensity along the pixel-rows and -columns within the image, treating them as individual signals. This technique utilises the less-constrained wavelet transform, instead of the Fourier transform, to decompose these signals. Ultimately, by computing the power spectra and determining the sizes (firstly in pixel, then changing to millimeter, using the scale) of the wavelet components (each corresponding to an individual grain), the user can derive the grain size distribution for the given image. Prior to this study, this methodology had demonstrated its efficiency as a non-DL image-processing technique for mixed sediments (Buscombe, 2013; 2020) and had previously been tested by us, under underwater conditions as well (Ermilov et al., 2020).

3 Results and discussion

3.1 Evaluation of the training

To evaluate the training process, the 2957 images of the validation set were analysed by the developed DL algorithm and its results were then compared to their human-annotated counterparts. Fig. 5a-d shows results of original images (from the validation set), their ground truth (annotation by the training personnel), as well as the DL prediction (result of the model). The overlays of the original and the predicted images are also shown for better visualization. Calculating the overall pixel accuracy (i.e., the percent of pixels that were correctly classified

during validation) returned a satisfactory result with an average 96% match (over the 2957 validation images, each having 960x540 resolution, adding up to a total of 1 532 908 800 pixels as 100%). As this parameter in object detection and DL is not a stand-alone parameter (i.e., it can still be high even if the model performs poorly), the mean IoU (intersection-over-union or Jaccard index) was also assessed, indicating the overlap of ground truth area and prediction area, divided by their union (Rahman and Wang, 2016). This parameter showed a much slighter agreement of 41.46%. Interestingly, there were cases, where the trained model gave better result than the annotating personnel. While this highlighted the importance of thorough and precise annotation work, it also showcased that the number of poor annotations was relatively low, so that the algorithm could still carry out correct learning process and later detections, while not being severely affected by the mistake of the training personnel. Fig. 5e showcases an example for this: the correct appearance of cobble (yellow) in the prediction, even though the user (ground truth) did not define it during annotation. As a matter of fact, these false errors also decrease the IoU evaluation parameter, even though they increase the performance of the DL algorithm on the long term. Hence, this shows that pure mathematical evaluation may not describe the model performance entirely. Considering that others also reported similar experience with DL (Lu et al., 2018) and the fact that 40% and 50% are generally accepted IoU threshold values (Yang et al., 2018; Cheng et al., 2018; Padilla et al., 2020), we considered the 41.46% acceptable, while noting that the annotation and thus the model can further be improved. The general quality of our underwater images may have also played a role in lowering the IoU result.
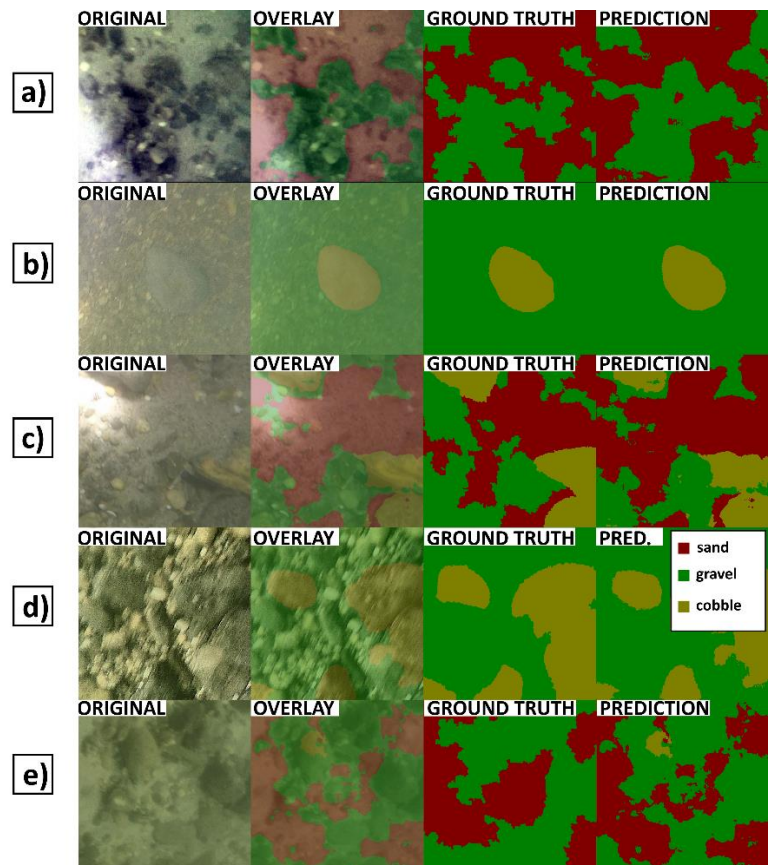
Figure 5: a-d) Example comparisons of ground truth (drawn by the annotating personnel, 3rd column) and DL predicted (result of analysing the raw image by the previously trained DL model, 4th column) during the validation process. The 1st column shows raw images, while the 2nd column overlays the result of the DL detection on the raw image for better visual context. e) Example of training personnel mistake during the annotation (i.e., lack of cobble/yellow annotation in ground truth) and how the DL performed better by hinting at the presence of the cobble fraction, leading to a false negative result during validation.

405 One of these quality issues for the DL algorithm was associated with the illumination. Using a diving light with

406 small beam divergence proved counterproductive. The high intensity, focused light occasionally caused

407 overexposed zones (white pixels) in the raw bed image, misleading the DL algorithm and resulting in detection

408 of incorrect classes there (Fig. 6a). In darker zones, where the suspended sediment concentration was higher and

409 at the same time, the effect of camera tilting was not completely removed by preprocessing, the focused light

410 sometimes reflected from the suspended sediment itself and resulted in brighter patches in the images (Fig. 6b).

411 This also caused false positive detections.

412
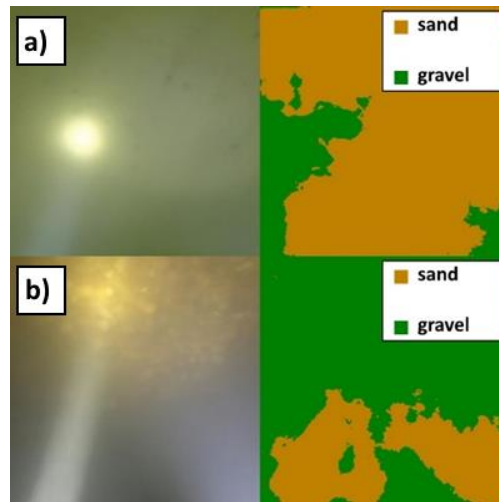
413
414 **Figure 6: The effect of strong diving light on the DL algorithm. a) Purely sand covered zone. b) Darker zone with**
415 **higher SSC. The original images are on the left, while the DL detections can be found on the right.**

416

417 **3.2 Comparison of methods**

418 In each masked image, the occurring percentage of the given class (i.e., the percentage of the pixels belonging to

419 that class/colour mask, compared to the total number of pixels in the image) was calculated and used as the fraction

420 percentage in that given sampling point. These sediment classes reconstructed by the DL algorithm were then

421 compared to three alternative results: i) visual estimation, ii) GSD resulted from conventional grab sampling, iii)

422 wavelet-based image-processing. In the followings, results from two cross-sections will be highlighted, one from

423 Site A, the video used for the training, and one from Site B, being new for the DL. An averaging window of 15 m

424 was applied on each cross-sectional DL result to smoothen and despike the dataset. The interval of physical sample

425 collection in wider rivers can range anywhere between 20-200 m within a cross-section, depending on the river

426 width and the homogeneity of riverbed composition. The averaging window size was chosen to be somewhat

427 lower than our average applied physical sampling intervals in this study, but still in the same order of magnitude.

428 The scope of the present study did not include further sensitivity analysis of the window size. In the followings,

429 the reader is led through the comparison process via the example of two transects, and is given the over-all

430 evaluation of the accuracy of the method.

3.2.1 Visual evaluation and physical samples

In Fig. 7a, we depict the vessel's trajectory within Section A – II at Site A. The path is color-coded based on our visual assessment of the riverbed images, with distinct colors representing the prevalent sediment type at each specific location on the riverbed. Additionally, we have marked the positions of physical bed material samples with yellow markers for reference. App. Fig. A1 presents the unprocessed results of the DL detection for each analysed image along Section A – II, prior to any moving-average smoothing. It's important to note that our current approach is highly sensitive, occasionally resulting in substantial fluctuations in DL detection between successive, slightly displaced video frames. Owing to this sensitivity and the inherent uncertainty in the coordinates of the underwater photos and their corresponding physical samples, we discourage making direct comparisons by selecting a specific image and its DL detection. Instead, we have implemented a moving-average-based smoothing technique for each raw, cross-sectional DL detection, using a window size of 15 meters at each site. These moving averages serve as the basis for comparisons with the physical sampling data and the wavelet method. For the sake of clarity, we have included the raw DL detections of all sampling point images in the Appendix, although these results may not precisely reflect their corresponding moving-average values. In Fig. 7b, we present a comparison between the cross-sectional visual classification and the DL-detected sediment fractions in percentage after applying the moving-average smoothing (i.e., the smoothed version of App. Fig. A1). Any noise observed in these results is primarily attributable to abrupt changes in lighting conditions, which can occur either when visual contact with the riverbed is momentarily lost due to sudden bathymetrical changes or as a result of increased suspended sediment concentration. Overall, our DL results exhibit a commendable concordance with human evaluations. For instance, in the vicinity of 100 meters from the left bank, between sampling points AII-1 and AII-2, the DL algorithm correctly identifies a peak with approximately 70% sand and 30% gravel. Moreover, on either side of this peak, a steep transition to gravel and a decline in sand content are observed, consistent with visual observations, which we have labelled as "sandy gravel" and "gravelly sand." The DL algorithm also accurately identifies mixed sediment zones on both riverbanks.
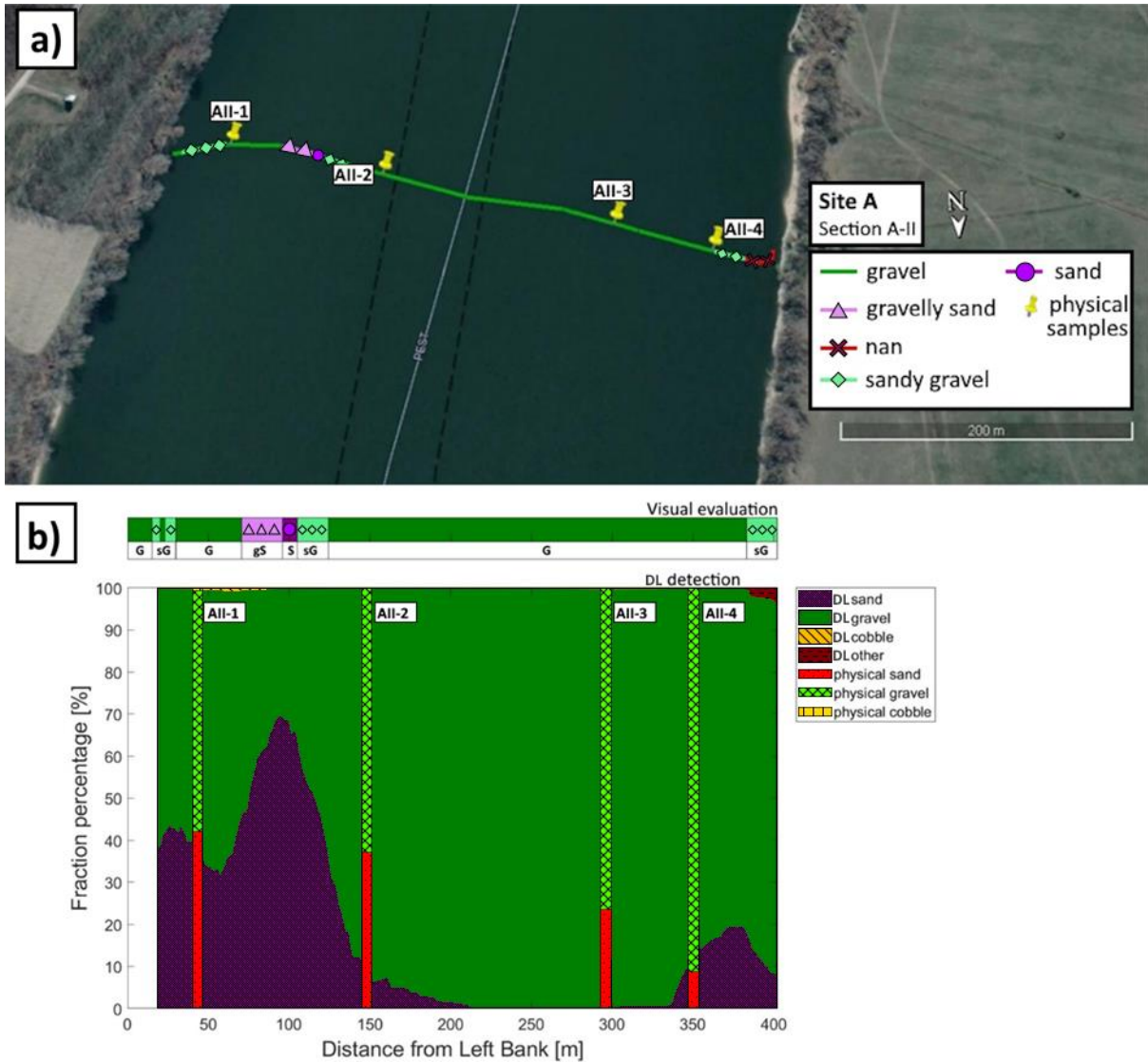
456

457 **Figure 7: a) The path of the vessel and camera in Section A – II, Site A. The polyline is coloured based on the sediment**
458 **features seen during visual evaluation of the video. Yellow markers are the locations of physical bed material samplings.**
459 **(Map created with Google Earth Pro). b) The visual evaluation of the dominant sediment features in the video (top)**
460 **compared to sediment fraction percentage, recognised by the DL algorithm (bottom). DL result after applying moving-**
461 **averaging. The visual evaluation included four classes: gravel – G, sandy gravel – sG, gravelly sand – gS, sand – S,).**
462 **The fractions of the physical samples are shown as verticals.**

463

464 At site B (Fig. 8a) the river morphology is more complex compared to Site A as a groyne field is located along

465 the left bank (see Fig. 2b). As such, the low flow regions between the groynes yield the deposition of fine

466 sediments, and much coarser bed composition in the narrowed main stream. As it can be seen, the DL algorithm

467 managed to successfully distinguish these zones: the extension of fine sediments in the deposition zone at the left

468 bank were adequately estimated and showed a good match with the visual evaluation for the whole cross-section

469 (see Fig. 8b).

470
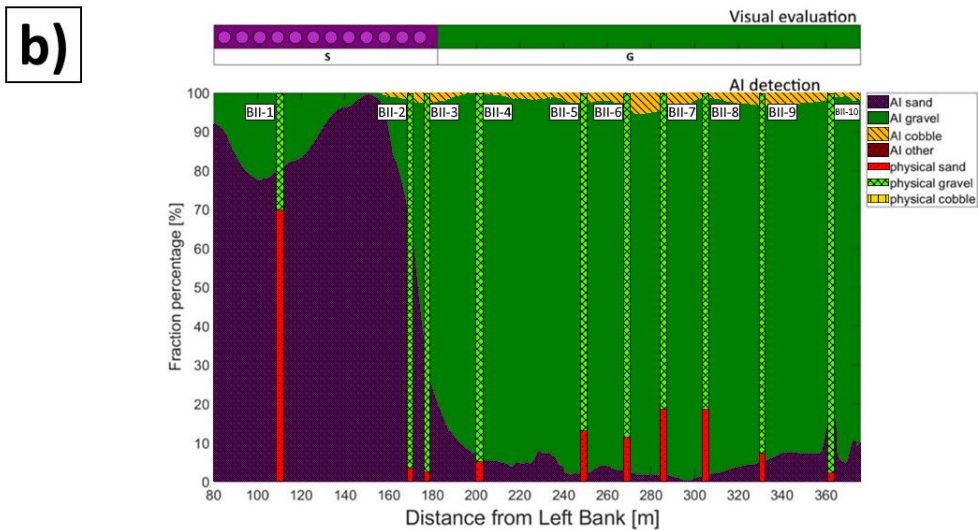
Figure 8: a) The path of the vessel and camera in Section–B – II, Site B. The polyline is coloured based on the sediment seen during visual evaluation of the video. Yellow markers are the locations of physical bed material samplings. (Map created with Google Earth Pro). b) Sediment fraction percentages in Section–B – II, recognised by the AI. The visual evaluation included two classes: gravel – G, sand – S). The fractions of the physical samples are shown as verticals.

Results of the other measurements can be found in the Appendix. App. Fig. C2, D2 and E2 show that the trend of riverbed composition from the visual evaluation is well-captured by the DL algorithm in the other cross-sections of the study as well.

Next, the physically measured and DL-detected relative proportion of sand, gravel and cobble fractions were compared in each of the 27 sampling points. Firstly, however, outliers or incomparable data had to be identified. In our case, this meant the separation of sampling points where the differences between the results of the two methods were independent from the efficiency and performance of the DL algorithm. This selection was carried out after analysing the grainsize distribution curves of the weight-sieved physical samples (App. Fig. F1) and the riverbed images around the sampling points (App. Fig. A3, B1, C4, D4, E4). Based on our findings, the outliers

have been identified and separated into Outlier Type A, and Outlier Type B categories. First category included the sampling points where the GSD curves showcased bimodal (gap graded) distributions. This type of riverbed sediment distribution is a typical sign of riverbed armouring (Rákóczi, 1987; Marion & Fraccarollo, 1997), where a coarse surface layer protects the underlying finer subsurface substrate (see e.g., Wilcock, 2005). While the camera only sees the upper layer, the bucket sampler can penetrate the surface and gather sample from the subsurface as well. As a result, the two methods cannot be compared solely on the surface distribution. In App. Fig. A2, supportive images of bed armouring are provided, taken during our surveys in the Upper section of the Hungarian Danube. Out of the 27 sampling points, 11 were affected by armouring and categorised as Outlier Type A. The category of Outlier Type B consisted of points from the opposite case: where the riverbed image contained fine sediment, but the physical samples did not. In these cases, a relatively thin layer of fine sediment covered the underlying gravel particles. 2 sampling points were categorised as Outlier Type B, both of which were near to the borderline between a deposition zone behind a groyne, and the gravel bedded main channel. In these cases, the bucket sampler probably either stirred up the deposited fine sediment and washed it down during its lifting or was dragged through purely gravel bedded patch during sampling, as the surface composition was rapidly changing on this before-mentioned borderline. It is important to highlight that the analysis of physical samples involves measuring and weighing various sediment size classes, leading to weight distribution. In contrast, imaging methods offer surface distributions, and as a consequence, the presence of a thin layer of fine sediments on the surface can significantly skew the resulting composition (Bunte and Abt, 2001; Sime and Ferguson, 2003; Rubin et al., 2007).

	Comparable data	Outlier Type A	Outlier Type B	$\sum$
No. sampling points	14	11	2	27

Table 2: After evaluating the results of the sieving analyses and riverbed surface images, out of the 27 sampling points, 14 were defined as comparable between the applied sampling methods. 11 points were categorised as Outlier Type A, because their GSD curves were bimodal. 2 points were defined as Outlier Type B, since their images showed the presence of fine sediment, while the sieve analyses did not.

Overall, the DL-based classification agreed well within the comparable sampling points, with an average error of 4.5% (Fig. 9). It can be seen that even though in outlier points AII-1 and AI-3 the DL algorithm coincidentally gave good match with the sieving analysis, in the rest of the outlier points the DL- and physical-based results systematically differ from each other, supporting our outlier selection methodology.
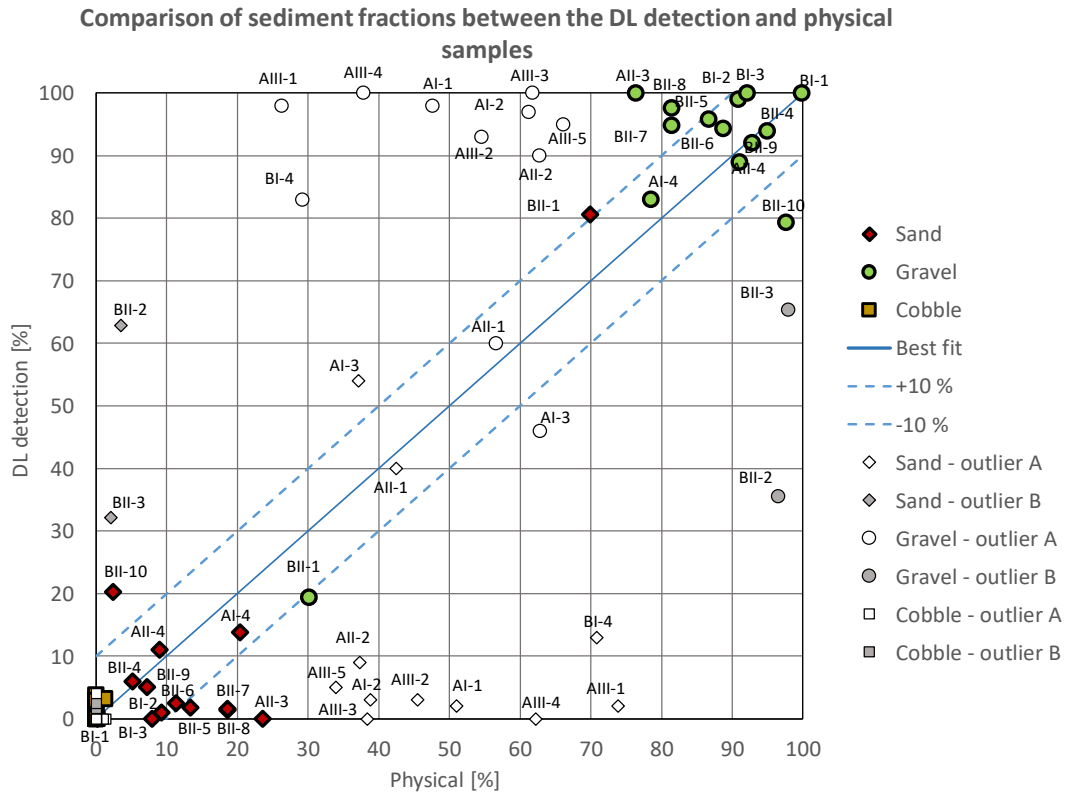
Figure 9: Comparison of relative sediment fractions between the DL detection and physical samples. The three main sediment types (sand-gravel-cobble) are marked with different colour and symbols. The name of the sampling points where the given relative proportion was measured/detected is also written for gravel and sand (cobble was negligible). The proportions of outlier sampling points are marked with white/grey, while the symbol represents the sediment type respectively. The comparable points have their proportions with green (gravel) and red (sand) symbols.

3.2.2 Wavelet analysis

Regarding the wavelet analysis-based imaging technique, it is evident that there is a slight overall overestimation of coarse particles, and the accurate reconstruction of sand classes is not achieved. This observation aligns with our earlier field experiences reported in Ermilov et al. (2020), where we highlighted the wavelet technique's pronounced sensitivity to image resolution. We demonstrated that to successfully detect a grain, its diameter must be at least three times larger than a pixel. In the subsequent analysis, we compare the sediment proportions determined by the wavelet-based method to those obtained earlier through DL and physical-based approaches, presenting the results in bar plots (Fig. 10, 11). For instance, when the camera was positioned closer to the riverbed at sampling points AII-1 and AII-4, resulting in a more favourable mm/pixel ratio, the wavelet algorithm was able to detect coarse sand accurately. However, it struggled to identify finer sand, leading to lower sand percentage estimates (Fig. 10). In other sampling points where sand particles were below the resolution limit, the wavelet method consistently identified the presence of cobbles instead (Fig. 10), a distinction not made by the other two methods. This pattern broadly characterizes the wavelet method's performance during our study. For illustrative purposes, we provide an example highlighting the differences in the capabilities of these two methods in Figure 12. While both methods detect the presence of two major sediment categories, the wavelet technique interprets

538 the information as a mixture of gravel and cobbles, whereas the DL algorithm recognizes the presence of sand

539 coverage and gravel particles.

540
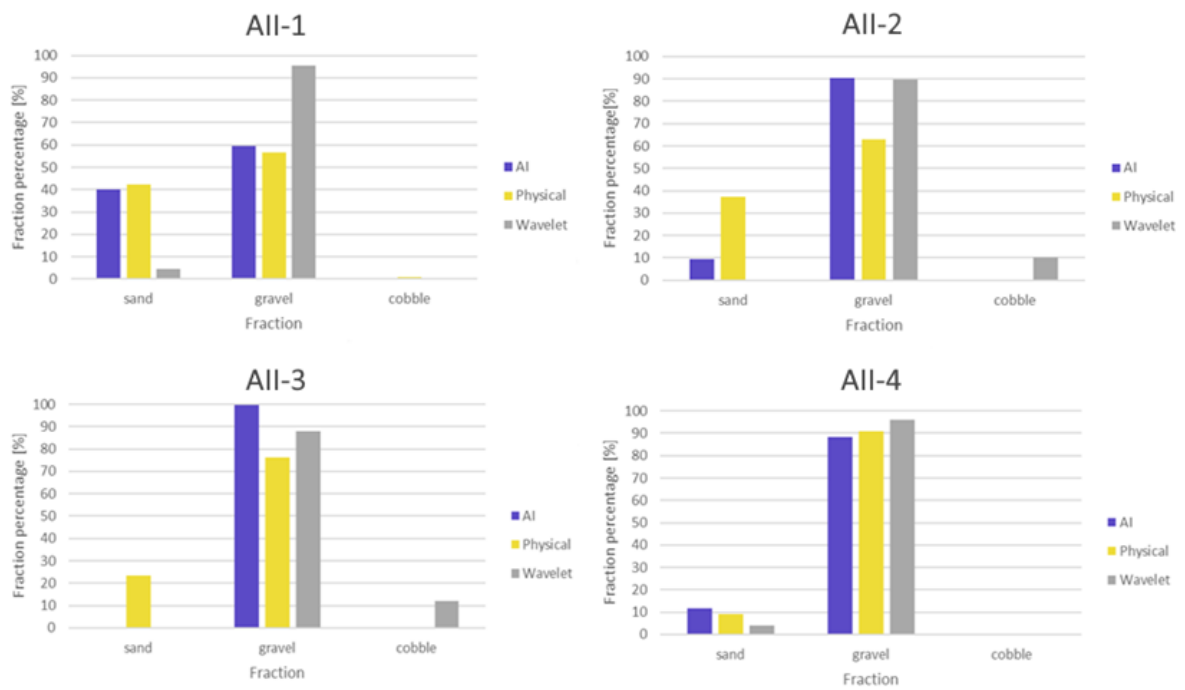
541
542 **Figure 10: Comparison of relative sediment fraction proportions [%] at the sampling locations from the moving-**
543 **averaged DL detection, conventional sieving and the wavelet-based image processing method. Section A – II.**

544
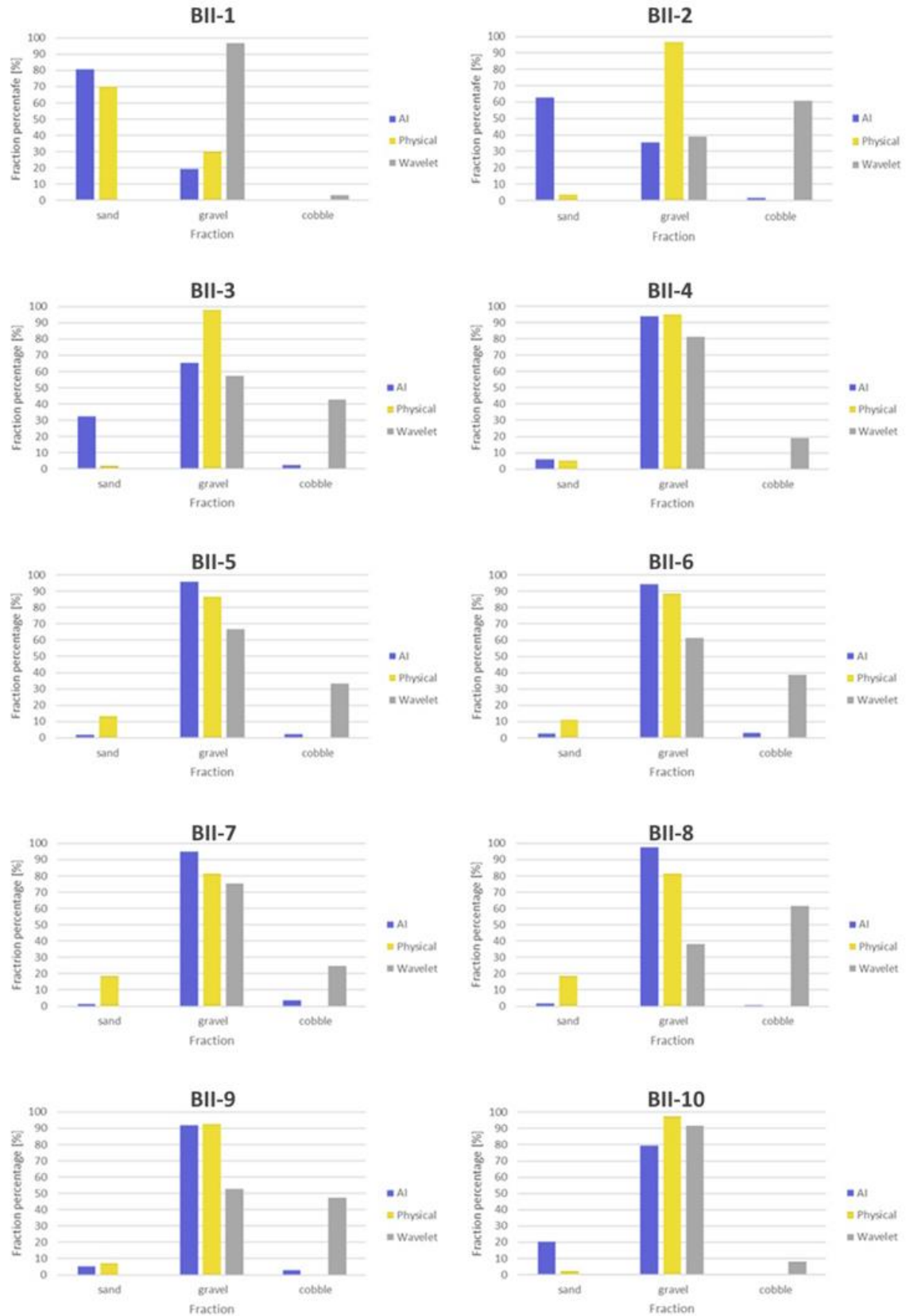
545
546 **Figure 11: Comparison of relative sediment fraction proportions [%] at the sampling locations from the moving-**
547 **averaged DL detection, conventional sieving and the wavelet-based image processing method. Section–B – II.**
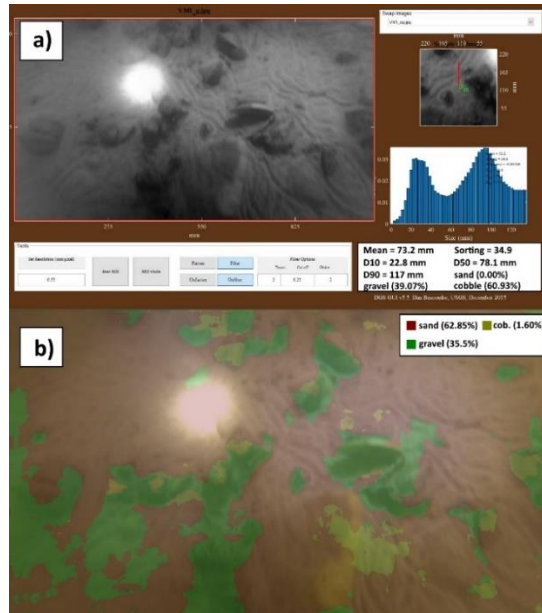
548

549 *Figure 12: a) Wavelet analysis result of the underwater image in BII-2. b) DL detection result of the same image.*

550

551 Overall, the comparison between the two image-based method showed greater discrepancies (Fig. 13), due to the

552 limitations of the wavelet approach, discussed earlier. The same sampling points were labelled as outliers as

553 earlier. As it can be seen, the wavelet significantly differed in the points where the physical samples and DL-

554 detections matched (green data points), due to its excessive, false cobble detections. However, it showed good

555 agreement with the DL in most of the outlier points, supporting the earlier observation: the surface in those points

556 was composed of solely gravel, and the finer fractions of the physical samples must have come from the

557 subsurface. Hence, the outlier selection process was well based.
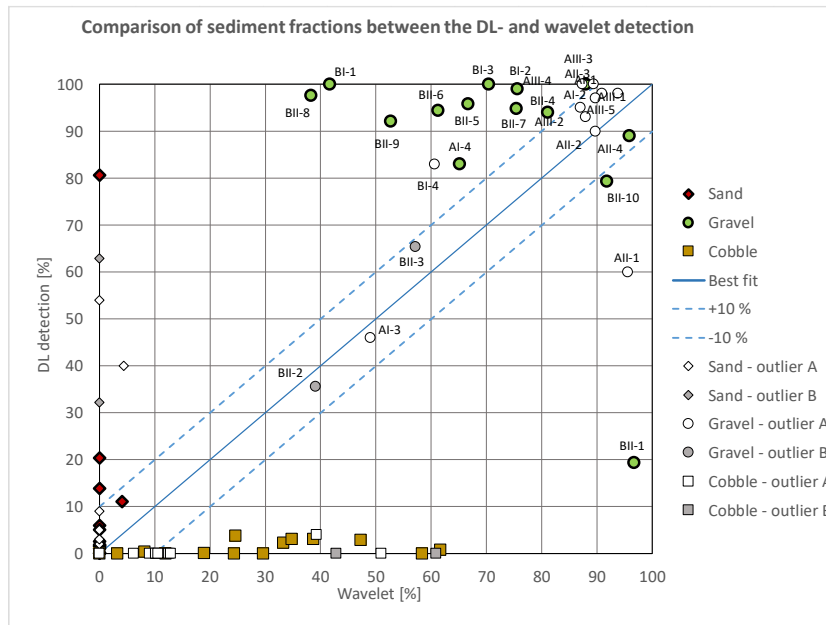
558

559 **Figure 13: Comparison of sediment fractions between the DL detection and the wavelet approach, for the selected**
560 **sampling points. The three main sediment types (sand-gravel-cobble) are marked with different colour (red-green-**
561 **yellow) and symbols (diamond-circle-square) respectively. The name of the sampling points where the given relative**
562 **proportion was measured/detected is also written for gravel. The proportions of outlier sampling points are marked**
563 **with white/grey, while the symbol represents the sediment type respectively. The comparable points have their**
564 **proportions with green (gravel), red (sand) symbols.**

565

566 Based on the results presented in this study, it could be established that the DL algorithm managed to recognise

567 the main features of the riverbed material composition from underwater videos with satisfactory accuracy in the

568 comparable sampling points (based on the sieving analysis of physical samples) and along cross-sections (based

569 on the visual evaluation). The method showed good potential for mapping heterogenous riverbeds along river

570 cross-sections. Furthermore, the wavelet proved to be a limited comparison tool with the introduced field

571 measurement methodology, as this latter did not provide it with the sufficient resolution most of the time.

572

573 **3.3 Implementation challenges**

574

575 The power supply for the entire imaging infrastructure, including the camera, diving lights, and lasers, relied on

576 batteries. However, due to the lower temperatures at the river bottom, the battery depletion rate was significantly

577 accelerated compared to typical conditions. To address this issue, we explored the option of a direct power supply

578 from the motorboat. Ensuring the camera's optimal positioning posed challenges as well. Proximity to the riverbed

579 risked damage to the equipment, while excessive camera-bed distances compromised image quality. To maintain

580 a clear view of the riverbed while avoiding blurry images, we utilized real-time ADCP water depth data to adjust

581 the camera's position, while simultaneously optimizing the boat's velocity. Increasing the recording frequency and

582 reducing exposure time emerged as potential solutions to mitigate this limitation. Lower vessel velocities were

583 not feasible, as they would have caused the vessel to drift out of the desired section. Alternatively, moving along

584 longitudinal (streamline) paths rather than transects may present the opportunity for slower vessel speeds,

585 potentially resulting in higher-quality images in the future. However, the conventional approach for river

586 bathymetry surveys typically involves transversal paths due to lower spatial variations along streamlines

587 compared to the transverse direction (Benjankar et al., 2015; Kinsman, 2015). Therefore, implementing

588 longitudinal paths may require a denser network to obtain sufficient data, thus increasing time demands. Hence,

589 careful consideration of path selection and interpolation methods becomes critical for this alternative approach.

590 Another challenge pertained to the impact of drag force on the measurement setup. Although the main body had

591 a streamlined design, the addition of other tools disrupted the setup's geometry. Additionally, we encountered a

592 slight imbalance in weight distribution. Long-term solutions could involve constructing a streamlined container

593 (e.g., a 3D-printed body or a body resembling unmanned underwater vehicles) with designated slots for each

594 device and improving weight distribution. Furthermore, we hypothesized that using lasers (as originally planned

595 in this study) during measurements could assist in orthorectifying the images, leveraging the known structure and

596 positioning of laser points' projections when the setup is perpendicular to the riverbed. This could reduce the

597 impact of occasional tilting, which may affect size analysis if scaling is included. In our specific case, we

598 demonstrated that the wavelet method had inherent limitations (e.g., image resolution limits) when applied within

599 our methodology, issues not attributable to camera tilting, as these would have had a significantly lower error

600 magnitude.

601

602 As for the training of the DL algorithm with the underwater images, the illumination is indeed a more crucial

603 aspect, compared to normal imagery methods. In many cases only the centre areas of the images were clearly

604 visible, whereas the remaining parts were rather dark and shady. Determining the boundaries between distinct

sediment classes for these images was challenging even for experienced eyes. This quality issue generated incorrect annotations at first. To overcome this issue, manually varying the white balance thus enhancing the visibility of the sediment could improve the results of the training. It is known that when DL methods are to be used, most of the problems arise from the data side (Yu et al., 2007), whereas issues related to the applied algorithms and hardware are rare. This is because data is more important from an accuracy perspective than the actual technical infrastructure (Chen et al., 2020). The time demand of image annotation (data preparation) is relatively high, i.e., a trained person could analyse roughly 10 images per hour. On the other hand, as introduced earlier, a great advantage of using DL is the capability of improving the quality of training itself, often yielding better agreement with reality, compared to the manual annotation. Similar results have been reported by Lu et al., (2018). This at the same time proves that with the introduced approach, there is no need for very precise manual training, thus a fast and effective training process can eventually be achieved.

The validation of the DL algorithm is far from straightforward. In this study, four approaches were adopted: a mathematical approach, and comparison with three other measurement methods, respectively. The mathematical approach was based on calculating pixel accuracy and the Intersection-over-union parameter, as it is usually done in case of DL methods to describe their efficiency (e.g., Rahman and Wang, 2016). However, the DL model in some cases overperformed, and provided more accurate results for the sediment composition than the human annotator did. This meant the calculated difference between the annotated validation images and their responding DL-generated result was not solely originated from underperformance of the DL-model, but from human error as well. Consequently, using only the mathematical evaluation in this study could not describe adequately the model performance. Hence, the results were compared to those of three other methods: i) visual evaluation of the image series, ii) a wavelet-based image-processing method (using the method of Buscombe, 2013) and iii) riverbed composition data from physical samples. Considering the features of the applied methods, the first one, i.e., the visual observation, is expected to be the most suitable for the model validation. Indeed, when assessing the bed surface composition by eye, the same patterns are sought, i.e., both methods focus on the uppermost sediment layer. On the other hand, the physical sampling procedure inherently represents subsurface sediment layers, leading to different grain size distributions in many cases. For instance, as shown earlier, if bed armour develops in the riverbed and the sampler breaks-up this layer, the resulted sample can contain the finer particles from the subsurface. On the contrary, in zones where a fine sediment layer is deposited on coarse grains, i.e., a sand layer on the top of a gravel bed, the physical samples represent the coarse material too, moreover, considering that the sieving provides weight distribution this sort of bias will even enhance the proportion of the coarse particles. Attempts were made to involve a third, wavelet-based method for model validation. However, this method failed when finer particles, i.e., sand, characterized the bed. This is an inherent limitation of these type of methods, as discussed earlier, i.e., when the pixel size is simply not fine enough to reconstruct the small grain diameters in the range below fine gravel. Lastly, the most comparable sample points were selected to quantify the performance of the DL. Holding the sieved physical samples as ground truth, the DL algorithm showed promising results. The average error (difference) between DL-detected and physically measured relative sediment fraction portion percentages was 4.5%. Furthermore, the DL algorithm successfully detected the trend of changing bed composition along complete river cross-sections.

As it is known, the ML and DL models can learn unknown relationships in datasets, but unwanted biases as well. With our current dataset, these biases would be the darker tones of visible grain texture and the lack of larger grain sizes. This way our model in its current state is only applicable effectively in the chosen study site, until the dataset is not expanded with additional images from other rivers or regions. However, the purpose of the study was to introduce the methodology itself and its potential in general and not to create a universal algorithm.

3.4 Novelty and future work

The introduced image-based DL algorithm offers novel features in the field of sedimentation engineering. First, to the authors' knowledge, underwater images of the bed of a large river have not yet been analysed by AI. Second, the herein introduced method enables extensive mapping of the riverbed composition, in contrast to most of the earlier approaches, where only several points or shorter sections were assessed with imagery methods. Third, the method is much faster compared to conventional samplings or non-DL-based image-processing techniques. The field survey of a 400 m long transect took ~15 minutes, while the DL analysis took 4 minutes (approx. 7 image/s). The speed range of 0.2-0.45 m/s of the measurement vessel and the 15 minutes per transect complies with the operating protocol of general ADCP surveys on rivers (e.g., RD Instruments, 1999; Simpson, 2002; Mueller and Wagner, 2013). Hence, the developed image-based measurement can be carried out together with the conventional boat-mounted ADCP measurements, further highlighting its time efficiency. Hence, the method offers an alternative approach for assessing riverbed material on-the-go, in underwater circumstances. As an extensive and quick mapping tool, it can support other types of bed material samplings in choosing the sampling locations and their optimal number. Furthermore, it can be used for quickly detecting areas of sedimentation and their extent, as we showed in Section 3.2. (e.g., Fig. 12b). This way, it can support decision-making regarding the maintenance of the channel or the bank-infiltrated drinking water production (detecting colmation zones). Fourth, a novel approach was used for the imaging and model training. As the camera-bed distance was constantly changing, the mm/pixel ratio also varied. Hence, no scale was defined for the algorithm beforehand. As we discussed in Section 1., earlier DL methods for sediment analysis (e.g., Soloy et al., 2020) all applied fixed camera heights and/or provided scaling for the AI. Furthermore, these studies were based on airborne measurements, mapping the dry zone of the rivers. In an underwater manner, it is extremely challenging to keep a fixed, constant camera height due to the spatially varying riverbed elevations. By avoiding the need for a scale, our method is faster and simpler to use. As a drawback, our method does not reconstruct detailed grainsize distributions, but rather measures the relative portions of the main sediment classes: sand, gravel, cobble. In short, this study showcased a fast bed material mapping tool, with a much denser spatial resolution than the conventional methods, saving up significant resources.

Originally, beside the three classes of main sediment types introduced in the study, others were also defined during annotation (e.g., bedrock, clams), but due to class imbalance (i.e., dominance of the three sediment classes), these were not discriminated successfully. In the future, improving the method through transfer learning (Zamir et al., 2018) using broader dataset and involving other sediment types will be considered. Another option for developing the method is to counter imbalance with the use of so-called weighted cross entropy (see Lu et al., 2019) on the current dataset, which will also be investigated.

684 Since the introduced method offers a quick way to provide extensive, spatially dense bed material information of
685 its composition, it can be used to boost the training dataset of predictive, ensemble bagging-based Machine
686 Learning techniques (e.g., Ren et al., 2020) and improve their accuracy. Furthermore, the method can support the
687 implementation of other imaging techniques. For instance, using one of the training videos of this study the authors
688 managed to reconstruct the grain-scale 3D model of a riverbed section with the Structure-from-Motion technique
689 (Ermilov et al., 2020), enabling the quantitative estimation of surface roughness. Underwater field cameras can
690 also be used for monitoring and estimating bedload transport rate (Ermilov et al., 2022) by adapting Large-scale
691 – Particle Image Velocimetry and the Statistical Background Model approach. This latter videography technique
692 may also be used with moving cameras (e.g., Hayman and Ekhlund, 2003), which enables its adaptation into our
693 method by e.g., detecting bedload movement in the cross-section.

695 The statistical representativity of the introduced method, as a surface sampling technique, needs to also be
696 addressed in future work. Following and building upon the experience of conventional, surface sampling
697 procedures (e.g., grid sampling; Diplas, 1988) may prove to be beneficial, where they provided the exact number
698 of gravel particles needed to be included (Wolman, 1954) to satisfy the representativity criteria. Then, using edge-
699 and blob-detection would enable to calculate and compare the number of gravel particles in the images to this
700 value. Furthermore, we intend to apply 2 cameras, with overlapping FOVs for increasing the covered area (and
701 the representativity) during surveys. Besides, it would also improve the accuracy of the Structure-from-Motion
702 technique mentioned earlier.

703 **4 Conclusion**

704 We introduced a novel, AI-based method for riverbed sediment analysis. The method uses underwater images to
705 reconstruct spatial variations in sediment grain sizes. Trained and validated with ~15.000 underwater images
706 collected in a section of the Danube in Hungary, we showed that the method can map the riverbed along the
707 vessel's route at a high spatial density of approximately 60-100 overlapping sample images per meter. The method
708 does not require a scale and thus allows the distance between the camera and the riverbed to vary. In contrast to
709 conventional point samples of river-bed substrate, our method provides spatially continuous data, that can be
710 further enhanced (e.g., by interpolation) to 2D maps. The method can be applied in studies where dense
711 information about river-bed composition is required, such as riverine habitat studies, computational hydro- and
712 morphodynamic models, or analyses of river-restoration measures. **Financial support.** The first author
713 acknowledges the support of the ÚNKP-21-3 New National Excellence Programme of the Ministry for Innovation
714 and Technology, and the National Research, Development and Innovation Fund, Hungary.

715 **Code availability.** The code written and used in this study is available here.

716 **Data availability.** The dataset and results can be accessed using the following links:
717 link1; link2; link3.

Author contributions. GB developed the code and carried out the training process. AAE carried out the fieldwork, evaluated the results, did the laboratory analysis, and collaborated with GB in improving the images. SB oversaw and directed the project, while managing the financial- and equipment background.

Competing interest. The contact author has declared that none of the authors has any competing interest.

Acknowledgements. The authors would like to thank our students Dávid Koós, Gergely Tikász, Schrott Márton and our technicians István Galgóczy, István Pozsgai, Károly Tóth and András Rehák for fieldwork support.

References

Adams, J.: Gravel Size Analysis from Photographs. J. Hydraul. Div., 1979, 105, 1247–1255. doi/10.1061/JYCEAJ.0005283, 1979.

Anglin, D. R., Haeseker, S. L., Skalicky, J. J., Schaller, H., Tiffan, K. F., Hatten, J. R., et al.: Effects of Hydropower Operations on Spawning Habitat, Rearing Habitat, and Standing/Entrapment Mortality of Fall Chinook Salmon in the Hanford Reach of the Columbia River. US Fish and Wildlife Service, final Report. Available at: https://pubs.er.usgs.gov/publication/70179516, 2006.

Baranya, S., Fleit, G., Józsa, J., Szalóky, Z., Tóth, B., Czeglédi, I. and Erős, T.: Habitat mapping of riverine fish by means of hydromorphological tools. Ecohydrology, Volume 11, Issue 7 e2009. Available at: https://doi.org/10.1002/eco.2009 , 2018.

Barnard, P., Rubin, D., Harney, J. and Mustain, N.: Field test comparison of an autocorrelation technique for determining grain size using a digital beachball camera versus traditional methods. Sedimentary Geology, 201(1–2): 180–195., 2007.

Benjankar, R., Tonina, D., Mckean, J.: One-dimensional and two-dimensional hydrodynamic modelling derived flow properties: Impacts on aquatic habitat quality predictions. Earth Surf. Process. Landf. 2015, 40, 340–356.

Benkő, G., Baranya, S., Török, T. G., and Molnár, B.: Folyami mederanyag szemösszetételének vizsgálata Mély Tanulás eljárással drónfelvételek alapján (in English: Analysis of composition of riverbed material with Deep Learning based on drone video footages). Hidrológiai Közlöny, 100, 61–69., 2020.Manuscript
Breheret, A.: Pixel Annotation Tool. Av. at: https://github.com/abreheret/PixelAnnotationTool, 2017.

Bunte, K. and Abt, S. R.: Sampling Surface and Subsurface Particle-Size Distributions in Wadable Gravel- and Cobble-Bed Streams for Analyses in Sediment Transport, Hydraulics, and Streambed Monitoring; General Technical Report (GTR), U.S. Department of Agriculture, Forest Service, Rocky Mountain Research Station: Fort Collins, CO, USA, 2001.

Buscombe, D. and Masselink, G.: Grain size information from the statistical properties of digital images of sediment. Sedimentology, 56, 421–438. doi/10.1111/j.1365-3091.2008.00977.x, 2008.

Buscombe, D.: Transferable wavelet method for grain-size distribution from images of sediment surfaces and thin sections, and other natural granular patterns. Sedimentology, 60 1709–1732., 2013.

Buscombe, D., Grams, P. and Kaplinski, M.: Characterizing riverbed sediment using high-frequency acoustics: 1. Spectral properties of scattering. Journal of Geophysical Research: Earth Surface, doi: 10.1002/2014JF003189, 119:12, (2674-2691), 2014a.

Buscombe, D., Grams, P. and Kaplinski, M.: Characterizing riverbed sediment using high-frequency acoustics: 2. Scattering signatures of Colorado Riverbed sediment in Marble and Grand Canyons. Journal of Geophysical Research: Earth Surface, doi/full/10.1002/2014JF003191, 119:12, (2674-2691), 2014b.

769 Buscombe, D. and Ritchie, A. C.: Landscape Classification with Deep Neural Networks. Geosciences, 8, 244.
770 Available at: https://doi.org/10.3390/geosciences8070244 , 2018.
771
772 Buscombe, D.: SediNet: a configurable deep learning model for mixed qualitative and quantitative optical
773 granulometry optical granulometry. Earth Surface Processes and Landforms, 45, 638-651. DOI:
774 10.1002/esp.4760, 2020.
775
776
777 Chandler, J., Lane, S. N. and Ashmore, P.: Measuring river-bed and flume morphology and parameterising bed
778 roughness with a KODAK DCS460 digital camera. International Archives of Photogrammetry and Remote
779 Sensing, Vol. XXXIII, Part B7., 2000.
780
781 Chen, C., Zhang, P., Zhang, H., Dai, J., Yi, Y., Zhang, H. and Zhang, Y.: Deep Learning on Computational-
782 Resource-Limited Platforms: A Survey. Volume 2020, Article ID 8454327. Available at:
783 https://doi.org/10.1155/2020/8454327, 2020.
784
785 Chen, L., Zhu, Y., Isola, P., Papandreou, G., Schroff, F. and Adam, H.: Encoder-Decoder with Atrous Separable
786 Convolution for Semantic Image Segmentation. Proceedings of the European conference on computer vision
787 (ECCV) (pp. 801-818). https://arxiv.org/abs/1802.02611., 2018.
788
789 Cheng, D., Li, X., Li, W. H., Lu, C., Li, F., Zhao, H. and Zheng, W. S.: Large-Scale Visible Watermark Detection
790 and Removal with Deep Convolutional Networks. In book: Pattern Recognition and Computer Vision. First
791 Chinese Conference, PRCV, Guangzhou, China, Proceedings, Part III. DOI: 10.1007/978-3-030-03338-5_3,
792 2018.
793
794 Cheng, Z., and Liu, H.: Digital grain-size analysis based on autocorrelation algorithm. Sedimentary Geology, 327,
795 21-31. Available at: https://doi.org/10.1016/j.sedgeo.2015.07.008, 2015.
796
797 Chezar, H. and Rubin, D. M.: Underwater Microscope System. United States Patent Office, The United States of
798 America as represented by the Secretary of the Interior, US Patent No. 6,680,795 B2., 2004.
799
800 Church, M. A., McLean, D. G., and Wolcott, J. F.: Sediments transport in Gravel Bed Rivers. Chap.: Riverbed
801 Gravels: Sampling and Analysis. John Wiley and Sons, New York, 43–88, 1987.
802
803 Cui, G., Su, X., Liu, Y., & Zheng, S.: Effect of riverbed sediment flushing and clogging on river-water infiltration
804 rate: a case study in the Second Songhua River, Northeast China. Hydrogeology Journal, 29(2), 551–565.
805 https://doi.org/10.1007/s10040-020-02218-7, 2021.
806
807 Delong, M. D. and Brusven, M. A.: Classification and spatial mapping of riparian habitat with applications toward
808 management of streams impacted by nonpoint source pollution. Environmental Management, 15:565-571. DOI:
809 10.1007/BF02394745, 1991.
810
811 Detert, M. and Weitbrecht, V.: User guide to gravelometric image analysis by BASEGRAIN. In Advances in
812 Science and Research; Fukuoka, S., Nakagawa, H., Sumi, T., Zhang, H., Eds.; Taylor and Francis Group: London,
813 UK, 2013; pp. 1789–1795. ISBN 978-1-138-00062-9., 2013.
814
815 Diplas, P.: Sampling Techniques for Gravel Sized Sediments. Journal of Hydraulic Engineering. DOI:
816 10.1061/(ASCE)0733-9429(1988)114:5(484), 1988.
817
818 Ermilov, A.A., Baranya, S. and Török, G.T.: Image-Based Bed Material Mapping of a Large River. Water, 12,
819 916. Available at: https://doi.org/10.3390/w12030916, 2020.
820
821 Ermilov, A. A., Fleit, G., Conevski, S., Guerrero, M., Baranya, S., & Rüther, N.: Bedload transport analysis using
822 image processing techniques. ACTA GEOPHYSICA, 1895-6572 1895-7455. http://doi.org/10.1007/ s11600-022-
823 00791-x, 2022.
824
825 Fehr, R.: Einfache Bestimmung der Korngrössenverteilung von Geschiebematerial mit Hilfe der
826 Linienzahlanalyse (In English: Simple detection of grain size distribution of sediment material using line-count
827 analysis). Schweizer Ing. und Archit., 105, 1104–1109., 1987.
828

829   Ferdowsi, B., Ortiz, C. P., Houssais, M., & Jerolmack, D. J. (2017). Riverbed armouring as a granular segregation
830   phenomenon. Nature Communications 2017 8:1, 8(1), 1–10. https://doi.org/10.1038/s41467-017-01681-3
831

832   Fetzer, J., Holzner, M., Plötze, M. and Furrer, G.: Clogging of an Alpine streambed by silt-sized particles –
833   Insights from laboratory and field experiments. Water Research, Volume 126, Pages 60-69.
834   https://doi.org/10.1016/j.watres.2017.09.015, 2017.
835

836   Geist, D. R., Jones, J., Murray, C. J. and Dauble, D. D.: Suitability criteria analyzed at the spatial scale of redd
837   clusters improved estimates of fall chinook salmon (Oncorhynchus tshawytscha) spawning habitat use in the
838   Hanford Reach, Columbia River. Canadian Journal of Fisheries and Aquatic Sciences, 57: 1636-1646., 2000.
839

840   Gilcher, M. and Udelhoven, T.: Field Geometry and the Spatial and Temporal Generalization of Crop
841   Classification Algorithms—A Randomized Approach to Compare Pixel Based and Convolution Based Methods.
842   Remote Sens., 13, 775., 2021.
843

844   GOPRO Hero 4 Silver: User Manual. Available at: https://gopro.com/content/dam/help/hero4-
845   silver/manuals/UM_H4Silver_ENG_REVA_WEB.pdf, 2014.
846

847   GOPRO Hero 7 Black: User Manual. Available at: https://gopro.com/content/dam/help/hero7-
848   black/manuals/HERO7Black_UM_ENG_REVA.pdf, 2018.
849

850   Graham, D. J., Reid, I. and Rice, S. P.: Automated sizing of coarse-grained sediments: image-processing
851   procedures. Mathematical Geology, 37, 1–28. https://doi.org/10.1007/s11004-005-8745-x, 2005.
852

853   Graham, D. J. Rollet, A.J., Piégay, H. and Rice, S. P.: Maximizing the accuracy of image-based surface sediment
854   sampling techniques. Water Resour. Res., 46, W02508. https://doi.org/
855   10.1029/2008WR006940, 2010.
856

857   Grams, P. E., Topping, D. J., Schmidt, J. C., Hazel, J. E. and Kaplinski, M.: Linking morphody-namic response
858   with sediment mass balance on the Colorado River in Marble Canyon: Issues of scale, geomorphic setting, and
859   sampling design, J. Geophys. Res. Earth Surf., 118, 361–381, doi:10.1002/jgrf.20050., 2013.
860

861   Guerit, L., Barrier, L., Liu, Y., Narteau, C., Lajeunesse, E., Gayer, E., Métivier, F.: Uniform grain-size distribution
862   in the active layer of a shallow, gravel-bedded, braided river (the Urumqi River, China) and implications for paleo-
863   hydrology. Earth Surface Dynamics. 6. 1011-1021. DOI: 10.5194/esurf-6-1011-2018., 2018.
864

865   Guerrero, M., Rüther, N., Szupiany, R., Haun, S., Baranya, S. and Latosinski, F.: The Acoustic Properties of
866   Suspended Sediment in Large Rivers: Consequences on ADCP Methods Applicability. Water, 8, 13;
867   doi:10.3390/w8010013, 2016.
868

869   Haddadchi, A., Booker, D.J. and Measures, R.J.: Predicting riverbed substrate cover proportions across New
870   Zealand. Catena, Volume 163, pp. 130-146. Available at: https://doi.org/10.1016/j.catena.2017.12.014, 2018.
871

872   Hayman, E., Eklundh, J.: Statistical Background Subtraction for a Mobile Observer. Proceedings of the Ninth
873   IEEE International Conference on Computer Vision (ICCV 2003) 2-Volume Set 0–7695–1950–4/03, 2003.
874

875   He, F., Liu, T., Tao, D.: Control batch size and learning rate to generalize well: theoretical and empirical evidence.
876   Neural Information Processing Systems, 2019.
877

878   Ibbeken, H., and Schleyer, R.: Photo-sieving: A method for grain-size analysis of coarse-grained, unconsolidated
879   bedding surfaces. Earth Surf. Process. Landforms, 11, 59–77. Available at:
880   https://doi.org/10.1002/esp.3290110108, 1986.
881

882   Igathinathane, C., Melin, S., Sokhansanj, S., Bi, X., Lim, C .J., Pordesimo, L. O. and Columbus, E. P.: Machine
883   vision based particle size and size distribution determination of airborne dust particles of wood and bark pellets.
884   Powder Technol., 196, 202–212. Available at: https://doi.org/10.1016/j.powtec.2009.07.024, 2009.
885

886   Kellerhals, R. and Bray, D. I.: Sampling Procedures for Coarse Fluvial Sediments. J. Hydraul. Div., 97, 1165–
887   1180., 1971.
888

Kim, H., Han, J. and Han, T. Y.: Machine vision-driven automatic recognition of particle size and morphology in SEM images. Nanoscale, 12, 19461–19469. Available at: https://doi.org/10.1039/D0NR04140H, 2020.

Kinsman, N.: Single-Beam Bathymetry Data Collected in Shallow-Water Areas near Gambell, Golovin, Hooper Bay, Savoonga, Shishmaref, and Wales, Alaska 2012–2013; Department of Natural Resources. Division of Geological & Geophysical Surveys: Fairbanks, AK, USA, 2015.

Le, Q. V.: Building high-level features using large scale unsupervised learning. In Proceedings of the 2013 IEEE International Conference on Acoustics, Speech and Signal Processing, Vancouver, BC, Canada, pp. 8595–8598., 2013.

Leopold, L. B.: An Improved Method for Size Distribution of Stream Bed Gravel. Water Resour. Res., 6, 1357–1366. https://doi.org/10.1029/WR006i005p01357, 1970.

Limare, A., Tal, M., Reitz, M. D., Lajeunesse, E., and Métivier, F.: Optical method for measuring bed topography and flow depth in an experimental flume. Solid Earth, 2, 143–154, https://doi.org/10.5194/se-2-143-2011., 2011.

Lowe, D. G.: Distinctive Image Features from Scale-Invariant Keypoints. International Journal of Computer Vision, 60, pages 91–110, 2004.

Lu, S., Gao, F., Piao, Ch. and Ma, Y.: Dynamic Weighted Cross Entropy for Semantic Segmentation with Extremely Imbalanced Data. 2019 International Conference on Artificial Intelligence and Advanced Manufacturing (AIAM). doi: 10.1109/AIAM48774.2019.00053, 2019.

Mueller D. S., Wagner, Ch. R.: Measuring Discharge with Acoustic Doppler Current Profilers from a Moving Boat. USGS, Chapter 22 of Book 3, Section A. https://pubs.usgs.gov/tm/3a22/, 2009.

Muñoz-Mas, R., Sánchez-Hernández, J., McClain, M. E., Tamatamah, R., Mukama, S. C., & Martínez-Capel, F.: Investigating the influence of habitat structure and hydraulics on tropical macroinvertebrate communities. Ecohydrology and Hydrobiology, 19(3), 339–350. https://doi.org/10.1016/j.ecohyd.2018.07.005, 2019.

Mueller D. S., Wagner, Ch. R.: Measuring discharge with acoustic Doppler current profilers from a moving boat, version 2.0. https://www.researchgate.net/publication/284587353_Measuring_discharge_with_acoustic_-Doppler_current_profilers_from_a_moving_boat, 2013.

Muste, M., Baranya, S., Tsubaki, R., Kim, D., Ho, H., Tsai, H. and Law, D.: Acoustic mapping velocimetry. Water Resour. Res., 52, 4132–4150, doi:10.1002/2015WR018354., 2016.

Obodovskyi, O., Habel, M., Szatten, D., Rozlach, Z., Babiński, Z., Maerker, M.: Assessment of the Dnieper Alluvial Riverbed Stability Affected by Intervention Discharge Downstream of Kaniv Dam. Water, 12(4):1104. https://doi.org/10.3390/w12041104, 2020.

Padilla, R., Netto, S. M. and da Silva, E. A. B.: A Survey on Performance Metrics for Object-Detection Algorithms. Conference: 2020 International Conference on Systems, Signals and Image Processing (IWSSIP). DOI: 10.1109/IWSSIP48289.2020, 2020.

Perez, L. and Wang, J.: The Effectiveness of Data Augmentation in Image Classification using Deep Learning. arXiv preprint arXiv:1712.04621. Av. at: https://arxiv.org/abs/1712.04621. 2017., 2017.

Purinton, B. and Bookhagen, B.: Introducing PebbleCounts: A grain-sizing tool for photo surveys of dynamic gravel-bed rivers. Earth Surf. Dyn., 7, 859–877. https://doi.org/10.5194/esurf-7-859-2019, 2019.

Rákóczi, L.: Selective erosion of noncohesive bed materials. Geografiska Annaler. Series A, Physical Geography, Vol. 69, No. 1, pp. 29-35. https://doi.org/10.2307/521364, 1987.

Rákóczi, L.: Identification of river channel areas inclined for colmation, based on the analysis of bed material. Vízügyi Közlemények, LXXIX., chapter 3., 1997.

947 Rahman, M. A. and Wang, Y.: Optimizing Intersection-Over-Union in Deep Neural Networks for Image
948 Segmentation. In: Bebis G. et al. (eds) Advances in Visual Computing. ISVC 2016. Lecture Notes in Computer
949 Science, vol 10072. Springer, Cham. https://doi.org/10.1007/978-3-319-50835-1_22, 2016.

951 RD Instruments – Acoustic Doppler Current Profilers – Appliction Note: https://www.comm-
952 tec.com/library/Technical_Manuscripts/RDI/FSA-004%20Mode1.pdf, 1999.

954 Rice, S. and Church, M.: Grain size along two gravel-bed rivers: Statistical variation, spatial pattern and
955 sedimentary links. Earth Surf. Process. Landf., 23, 345–363., 1998.

957 Ren, H., Hou, Z., Duan, Z., Song, X., Perkins, WA., Richmond, M. C., Arntzen, E. V. and Scheibe, T. D.: Spatial
958 Mapping of Riverbed Grain-Size Distribution Using Machine Learning. Front. Water, 2:551627. doi:
959 10.3389/frwa.2020.551627, 2020.

961 Rozniak, A., Schindler, K., Wegner, J. D. and Lang, N.: Drone images and Deep Learning for river monitoring in
962 Switzerland. Semester project. Institute of Geodesy and Photogrammetry, Project, Swiss Federal Institute of
963 Technology (ETH) Zurich, 2019.

965 Rubin, D. M.: A simple autocorrelation algorithm for determining grain-size from digital images of sediment. J.
966 Sed. Res., 74, 160–165., 2004.

968 Rubin, D. M., Chezar, H., Harney, J. N., Topping, D. J., Melis, T. S., Sherwood, C. R.: Underwater microscope
969 for measuring spatial and temporal changes in bed-sediment grain size. Sedimentary Geology, Volume 202, Issue
970 3, Pages 402-408, https://doi.org/10.1016/j.sedgeo.2007.03.020, 2007.

972 Scheder, C., Lerchegger, B., Flödl, P., Csar, D., Gumpinger, C. and Hauer, C.: Riverbed stability versus clogged
973 interstitial: Depth-dependent accumulation of substances in freshwater pearl mussel (Margaritifera margaritifera
974 L.) habitats in Austrian streams as a function of hydromorphological parameters. Limnologica, Volume 50,
975 January 2015, Pages 29-39. https://doi.org/10.1016/j.limno.2014.08.003, 2015.

977 Shields, F. D., Jr. and Rigby, J. R.: River habitat quality from river velocities measured using acoustic Doppler
978 current profiler. Environ. Manage.; 36(4):565-75. doi: 10.1007/s00267-004-0292-6., 2005.

980 Shields, F. D. Jr.: Aquatic Habitat Bottom Classification Using ADCP. Journal of Hydraulic Engineering, Vol.
981 136, Issue 5, 2010.

983 Sime, L. C. and Ferguson, R. I.: Information on grain-sizes in gravel bed rivers by automated image analysis. J.
984 Sed. Res., 73, 630–636., 2003.

986 Simpson, M. R.: Discharge Measurements Using a Broad-Band Acoustic Doppler Current Profiler. USGS, Open-
987 File Report 01-1, https://pubs.usgs.gov/of/2001/ofr0101/, 2002.

989 Singer, M. B.: A new sampler for extracting bed material sediment from sand and gravel beds in navigable rivers.
990 Earth Surface Processes and Landforms 33(14):2277 – 2284 DOI: 10.1002/esp.1661, 2008.

992 Soloy, A., Turki, I., Fournier, M., Costa, S., Peuziat, B. and Lecoq, N.: A Deep Learning-Based Method for
993 Quantifying and Mapping the Grain Size on Pebble Beaches. Remote Sens., 12, 3659, doi:10.3390/rs12213659,
994 2020.

996 Staudt, F., Mullarney, J. C, Pilditch, C. A. and Huhn, K.: Effects of grain-size distribution and shape on sediment
997 bed stability, near-bed flow and bed microstructure. Earth Surface Processes and Landforms, 44(5). DOI:
998 10.1002/esp.4559, 2018.

1000 Sun, Z., Zheng, H. and Sun, L.: Analysis on the Characteristics of Bed Materials in the Jinghong Reservoir on the
1001 Lancang River. Sustainability, 13, 6874. https://doi.org/10.3390/su13126874, 2021.

1003 Takechi, H., Aragaki, S. and Irie, M.: Differentiation of River Sediments Fractions in UAV Aerial Images by
1004 Convolution Neural Network. Remote Sens., 13, 3188. https://doi.org/10.3390/rs13163188, 2021.
1005

Taravat, A., Wagner, M. P., Bonifacio, R. and Petit, D.: Advanced Fully Convolutional Networks for Agricultural Field Boundary Detection. Remote Sens., 13, 722., 2021.

Török, G. T., Baranya, S. (2017) Morphological Investigation of a Critical Reach of the Upper Hungarian Danube. Periodica Polytechnica Civil Engineering. 61(4), pp. 752–761. https://doi.org/10.3311/PPci.10530, 2017.

USDA: Guidelines for Sampling Bed Material. Technical Supplement 13A, 2007.

Vanoni, V. A. and Hwang, L. S.: Relation between Bed Forms and Friction in Streams. J. Hydraulics Division., 93 (3), 121–144. doi:10.1061/JYCEAJ.0001607, 1967.

Verdú, J. M., Batalla, R. J. and Martinez-Casanovas, J. A.: High-resolution grain-size characterisation of gravel bars using imagery analysis and geo-statistics. Geomorphology, 72, 73–93., 2005.

Warrick, J. A., Rubin, D. M., Ruggiero, P., Harney, J. N., Draut, A. E. and Buscombe, D.: Cobble cam: Grain-size measurements of sand to boulder from digital photographs and autocorrelation analyses. Earth Surf. Process Landf., 34, 1811–1821. https://doi.org/10.1002/esp.1877, 2009.

Wilcock, P. R.: Persistance of armor layers in gravel-bed streams. Hydrology and Land Surface Studies. https://doi.org/10.1029/2004GL021772, 2005.

Wolcott, J. F., Church, M.: Strategies for sampling spatially heterogeneous phenomena: The example of river gravels. Journal of Sedimentary Research. v. 61, no. 4, p. 534–543, 1991.

Wolman, M. G.: Method of sampling coarse river bed material. Trans. Am., Geophysical Union, 35(6), 951-956.

WMO: Measurement of river sediments: prepared by the Rapporteur on Sediment Transport of the Commission for Hydrology. Report, World Meteorological Organization - No. 561, Operational hydrology report (OHR)- No. 16, 1981.

Xiao, Y., Li, W., & Yang, S.: Hydrodynamic-sediment transport response to waterway depth in the Three Gorges Reservoir, China. Arabian Journal of Geosciences, 14(775). https://doi.org/10.1007/s12517-021-07090-7/Published, 2021.

Yang, F., Yi, M., Cai, Y., Blasch, E., Sullivan, N., Sheaff, C., Chen, G. and Ling, H.: Multitask Assessment of Roads and Vehicles Network (MARVN). Proceedings Volume 10641, Sensors and Systems for Space Applications XI, 106410D, https://doi.org/10.1117/12.2305972, 2018.

You, K., Long, M., Wang, J., Jordan M.I.: How Does Learning Rate Decay Help Modern Neural Networks? https://doi.org/10.48550/arXiv.1908.01878, 2019.

Yu, L., Wang, S. and Lai, K.K.: Data Preparation in Neural Network Data Analysis. In book: Foreign-Exchange-Rate Forecasting with Artificial Neural Networks. DOI: 10.1007/978-0-387-71720-3_3, 2007.

Zamir, A. R., Sax, A., Shen, W., Guibas, L., Malik, J. and Savarese, S.: Taskonomy: Disentangling Task Transfer Learning. In Proceedings of the 2018 IEEE/CVF Conf. on Computer Vision and Pattern Recognition, Salt Lake City, UT, USA, pp. 3712–3722. doi: 10.1109/CVPR.2018.00391, 2018.

Zhang, Q., Shi, Y., Chen, Z. and Jiang, T.: ADCP measured flow current of the middle-lower Changjiang River channel. Front. Earth Sci., China 2, 1–9. https://doi.org/10.1007/s11707-008-0016-y, 2008.

Zhou, Y., Lu, J., Jin, Z., Li, Y., Gao, Y., Liu, Y. and Chen, P.: Experimental Study on the Riverbed Coarsening Process and Changes in the Flow Structure and Resistance in the Gravel Riverbed Downstream of Dams. Front. Environ. Sci., https://doi.org/10.3389/fenvs.2021.611668, 2021.

Zhu, J., Park, T., Isola, P. and Efros, A. A.: Unpaired Image-to-Image Translation using Cycle-Consistent Adversarial Networks. arxiv, https://arxiv.org/abs/1703.10593, 2020.

1063   **Appendix**

1064   **Appendix A Site A - Section A – II**
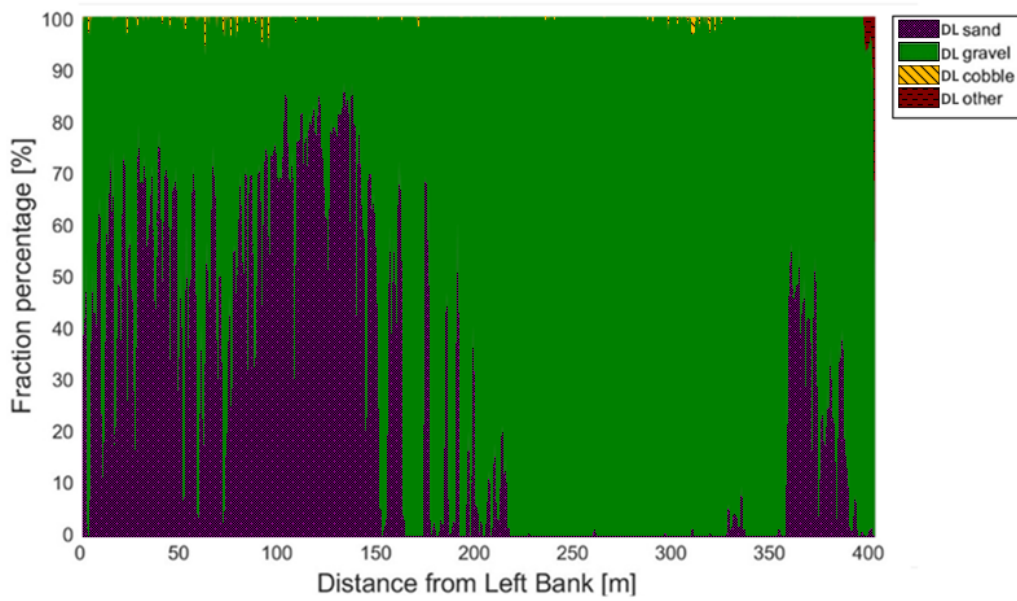
1065
1066   **Figure A1: The sediment fraction percentage results of every image, analysed by the DL algorithm along Section A -**
1067   **II. While the trends are apparent, the sensitivity of the method at its current state can be observed. DL result before**
1068   **applying moving-averaging.**

1069

1070
1071   **Figure A2: Images of bed armouring, taken during our surveys in the Upper section of the Hungarian Danube. We**
1072   **broke the surface armour to showcase the presence of the underlying finer fractions.**

1073
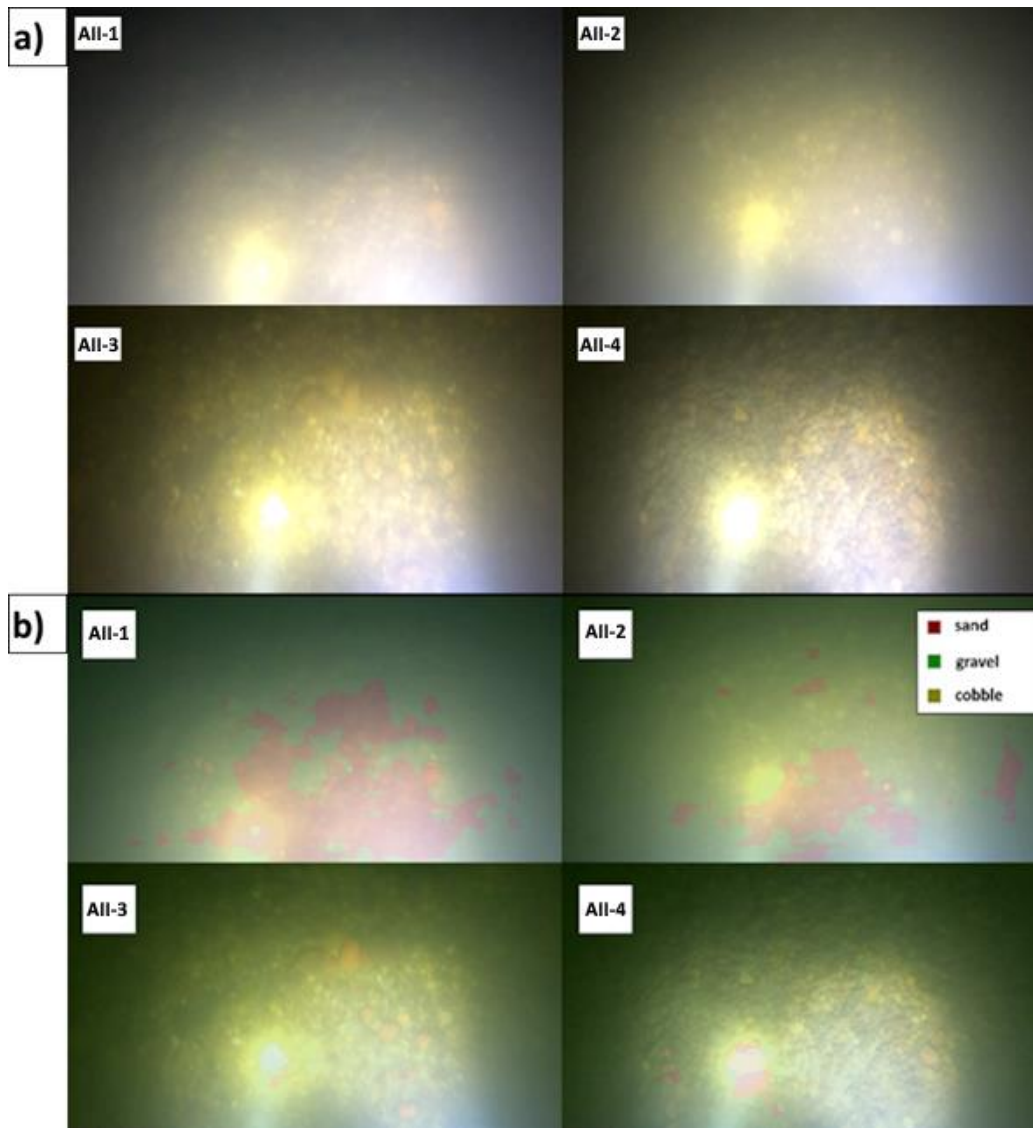
1074
1075 **Figure A3: a) Riverbed video images at the sampling points in Section A - II. b) Riverbed video images overlapped with**
1076 **their raw, DL detection result, at the sampling points in Section A - II.**

1077 **Appendix B Site B - Section B – II**
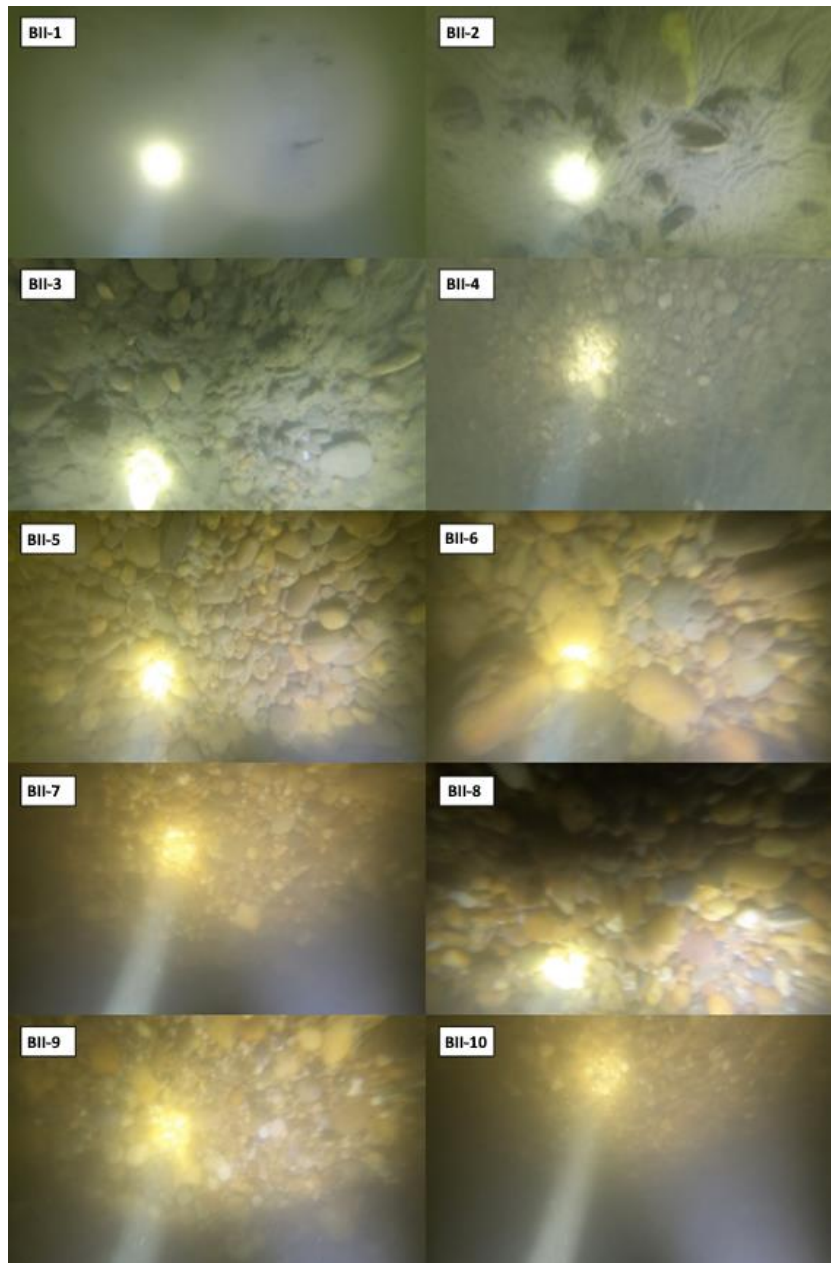
1078
1079 **Figure B1: Riverbed video images at the sampling points in Section B - II.**

1080
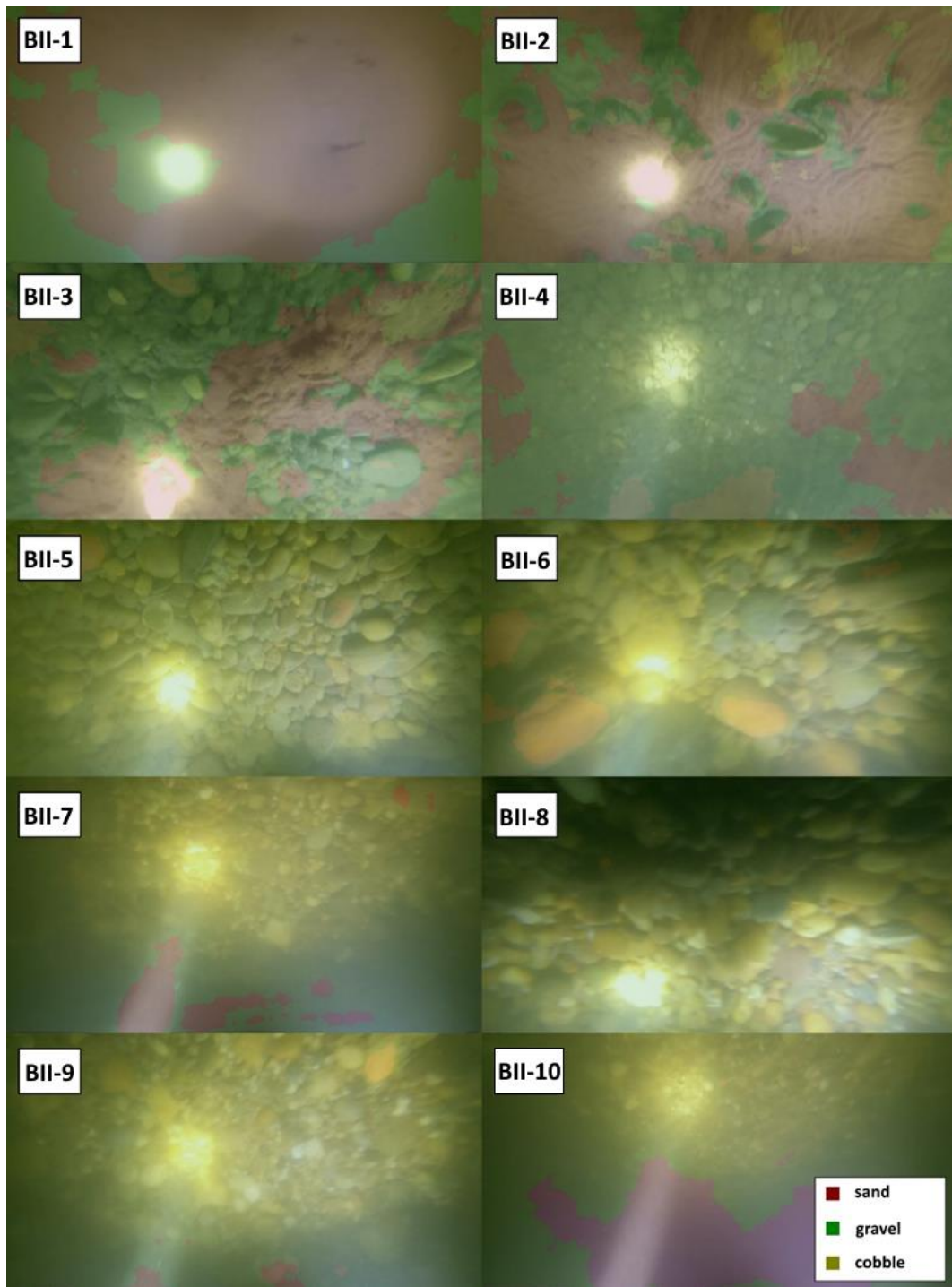
1081

1082 **Figure B2: Riverbed video images overlapped with their raw, DL detection result, at the sampling points in Section B**
1083 **- II.**

1084

1085 **Appendix C Site A - Section A – I**

1086
1087 Figure C1: The path of the vessel and camera in Section A - I, Site A. The polyline is coloured based on the sediment
1088 seen during visual evaluation of the video. Yellow markers are the locations of physical bed material samplings. (Map
1089 created with Google Earth Pro)

1090
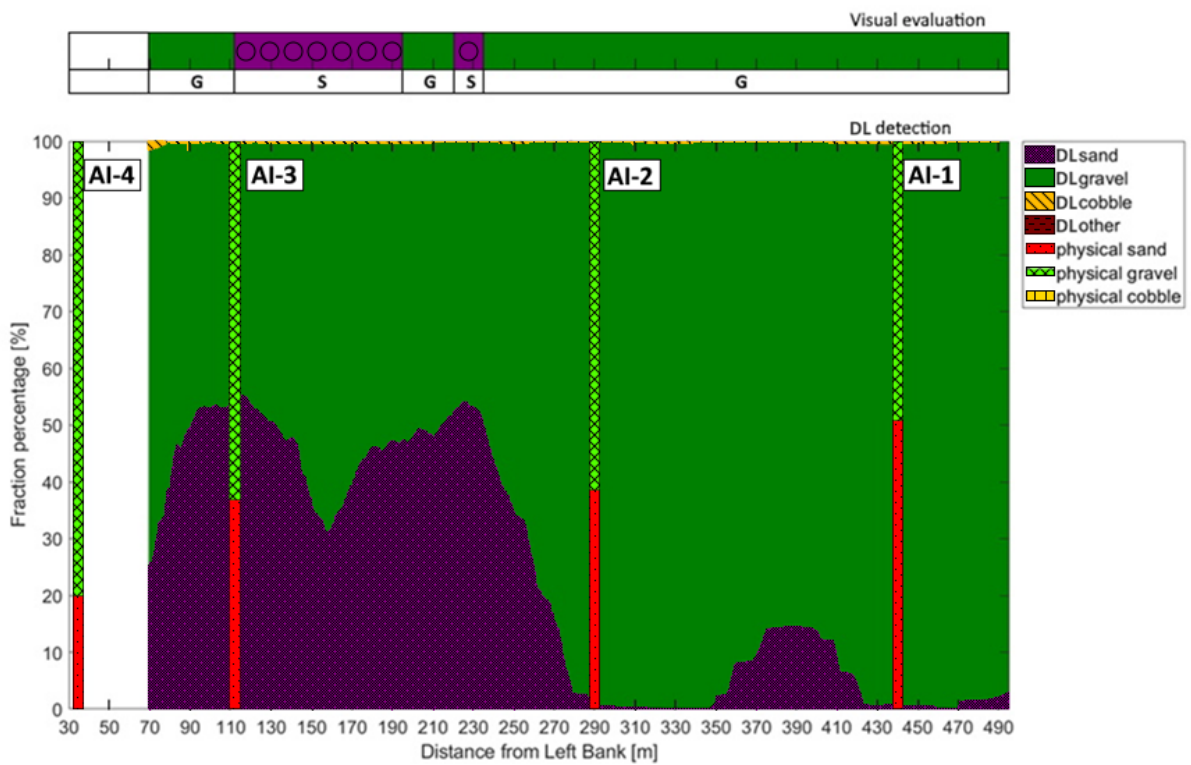
1091
1092 Figure C2: Sediment fraction percentages in Section A - I, recognised by the AI. The visual evaluation included two
1093 classes: gravel – G, sand – S). The fractions of the physical samples are shown as verticals.

1094
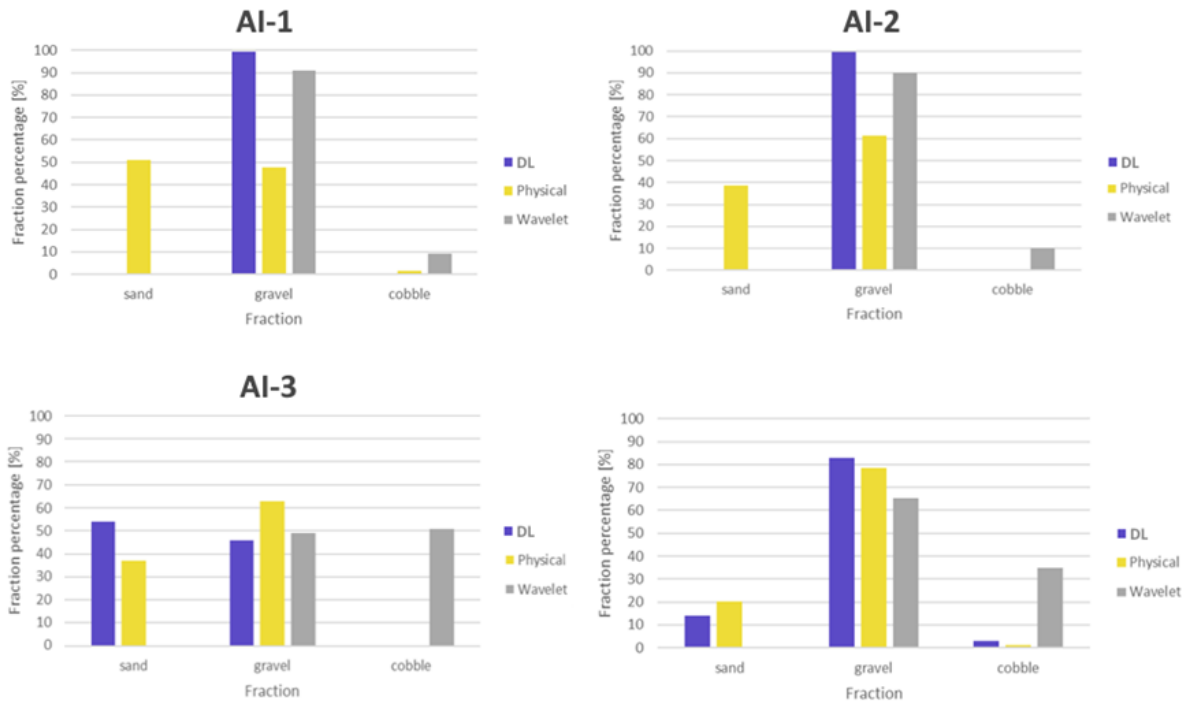
1095
1096 **Figure C3: Comparison of sediment fraction % at the sampling locations from the moving-averaged DL detection,**
1097 **conventional sieving and the wavelet-based image processing method. Section A - I.**
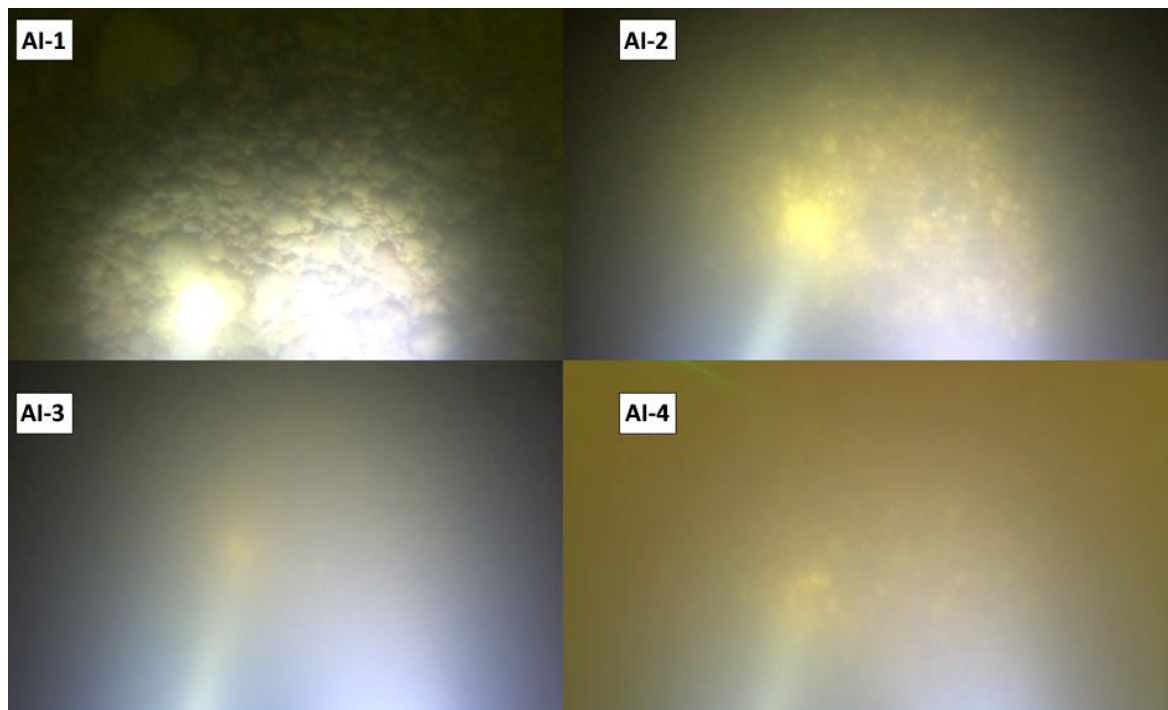
1098
1099 **Figure C4: Riverbed video images at the sampling points in Section A - I.**

1100
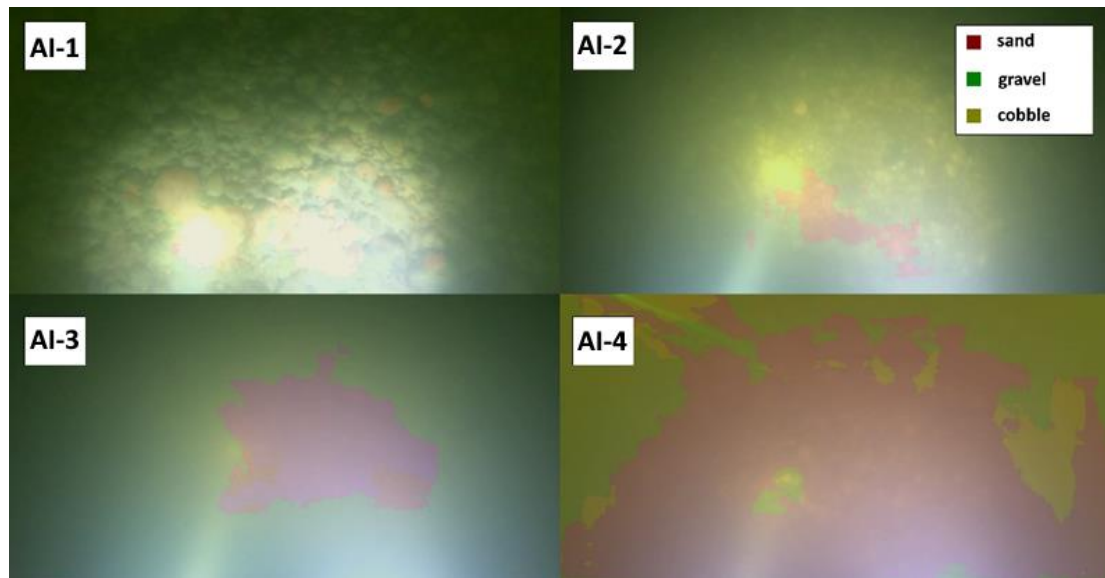
1101

1102   **Figure C5: Riverbed video images overlapped with their raw, DL detection result, at the sampling points in Section A**
1103   **- I.**

 Appendix D Site A – Section A - III
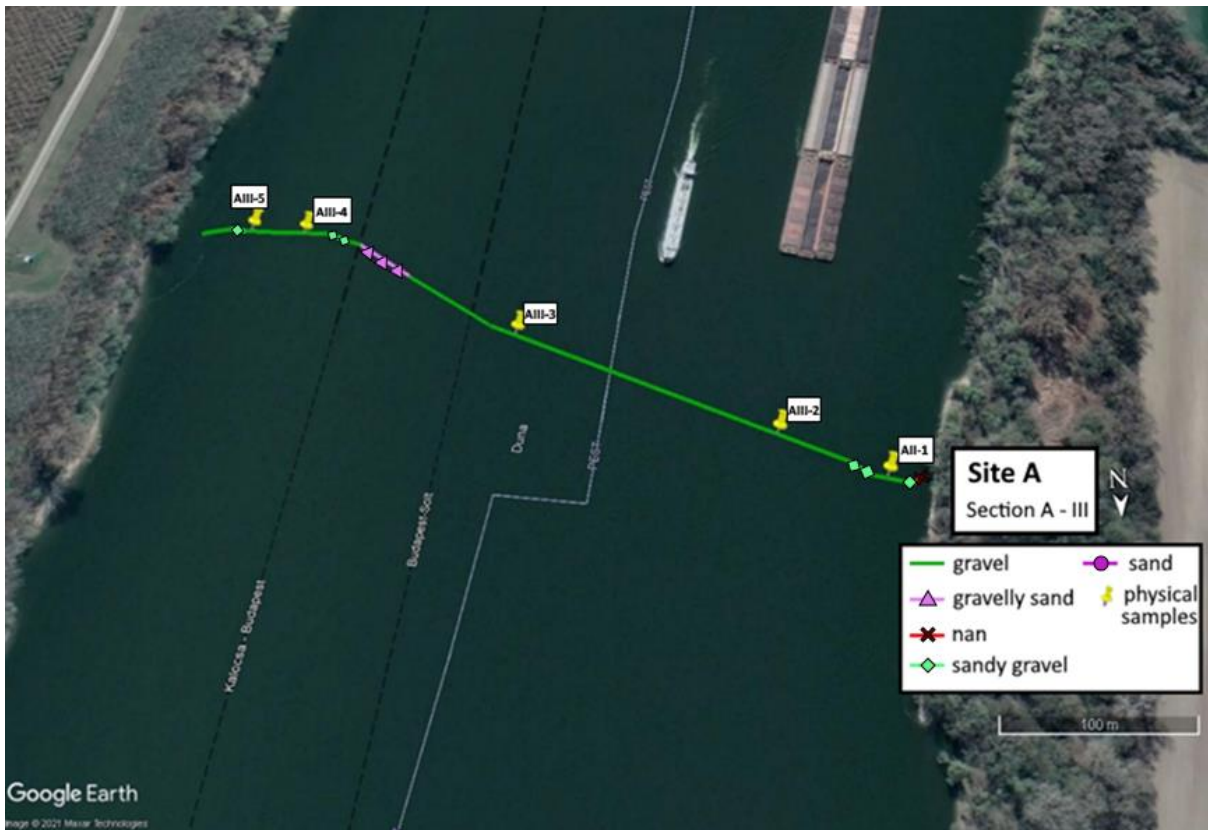
1105
1106 **Figure D1: The path of the vessel and camera in Section A - III, Site A. The polyline is coloured based on the sediment**
1107 **seen during visual evaluation of the video. Yellow markers are the locations of physical bed material samplings. (Map**
1108 **created with Google Earth Pro)**

1109
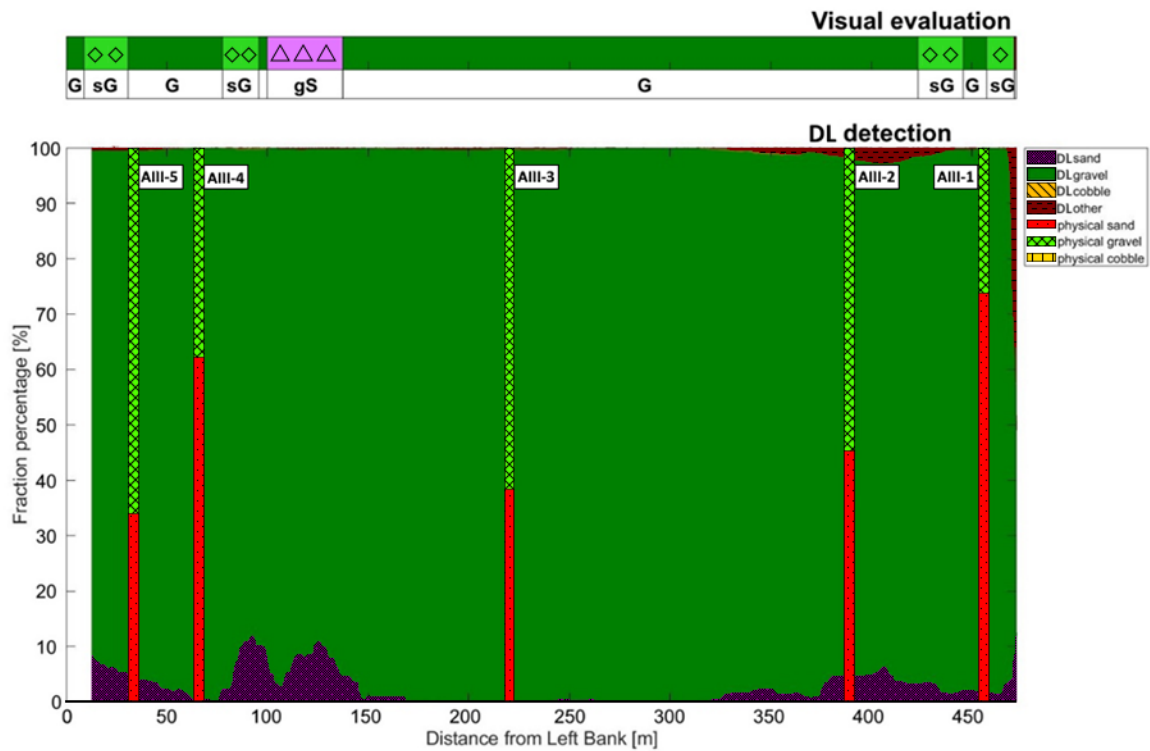
1110
1111 **Figure D2: Sediment fraction percentages in Section A - III, recognised by the AI. The visual evaluation included three**
1112 **classes: gravel – G, sandy gravel – sG, gravelly sand - gS). The fractions of the physical samples are shown as verticals.**
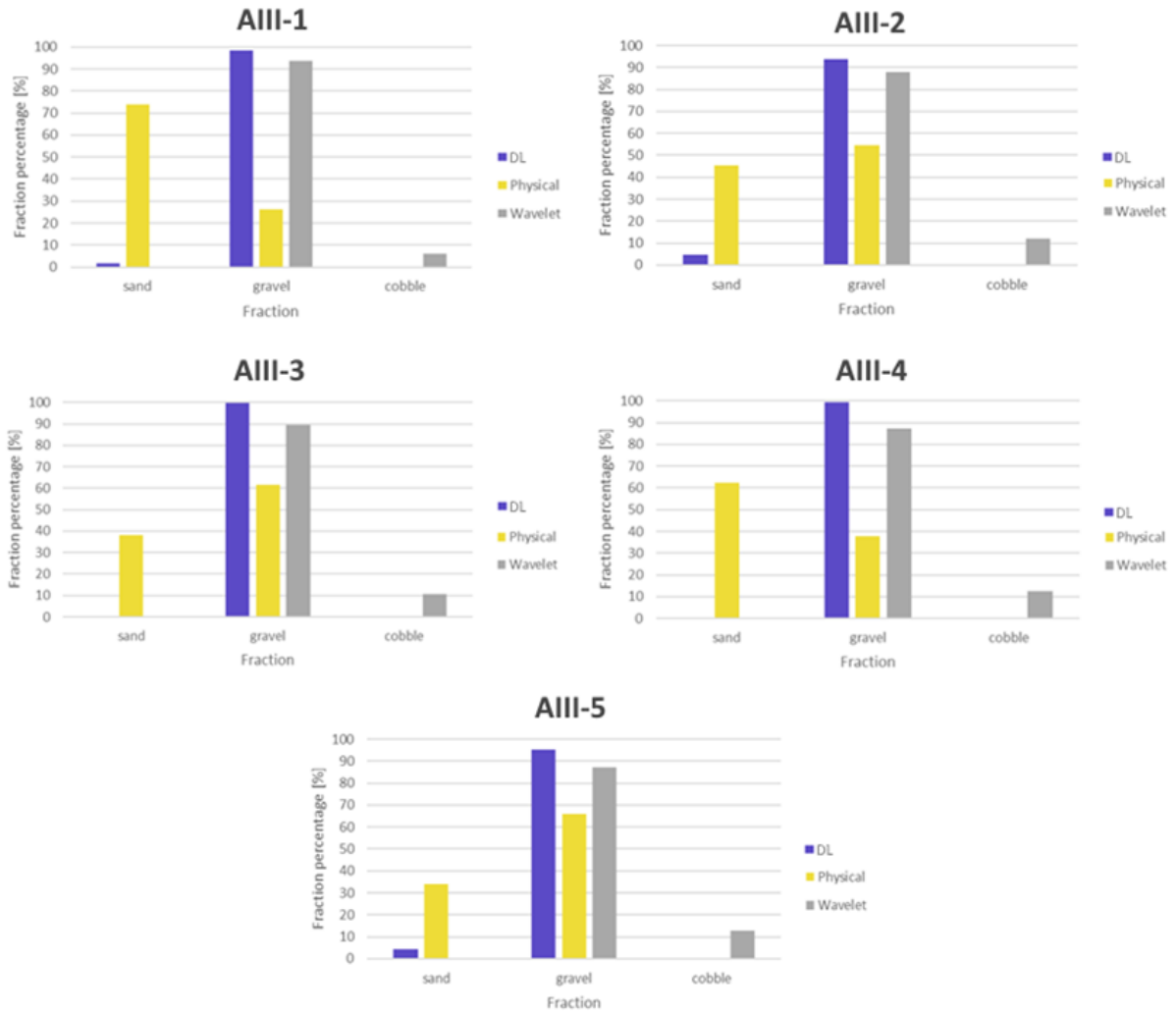
1114 **Figure D3: Comparison of sediment fraction % at the sampling locations from the moving-averaged DL detection,**
1115 **conventional sieving and the wavelet-based image processing method. Section A - III.**
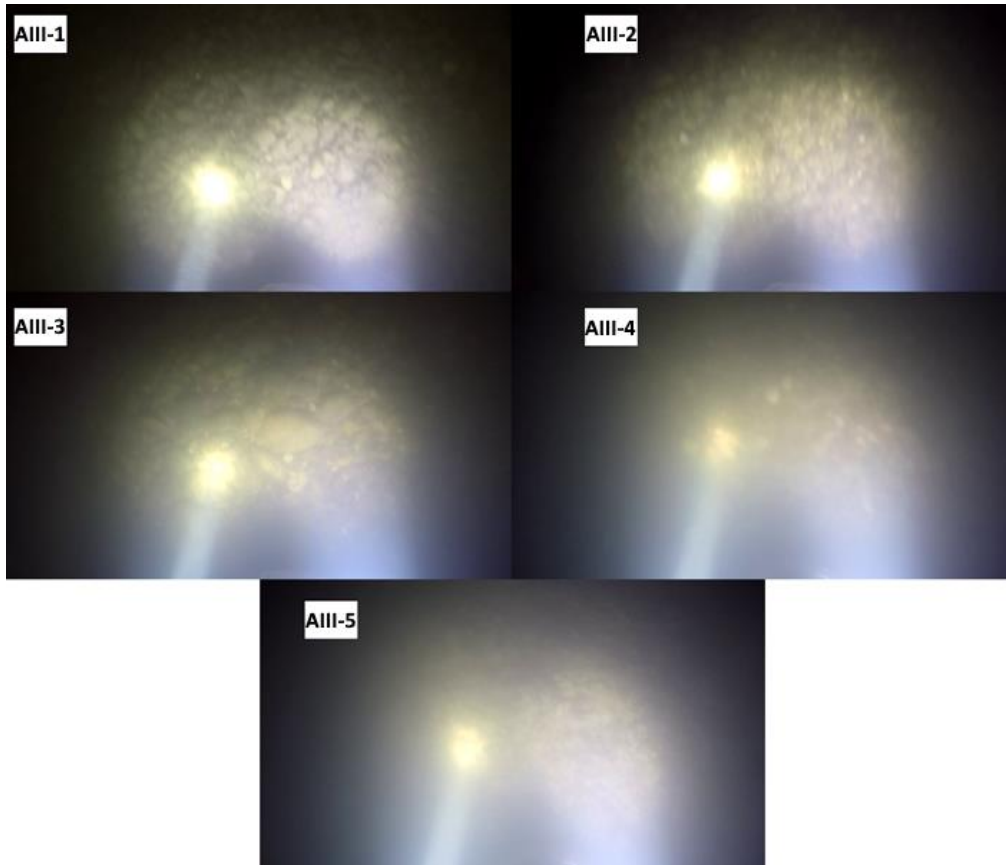
1116
1117 **Figure D4: Riverbed video images at the sampling points in Section A - III.**

1118
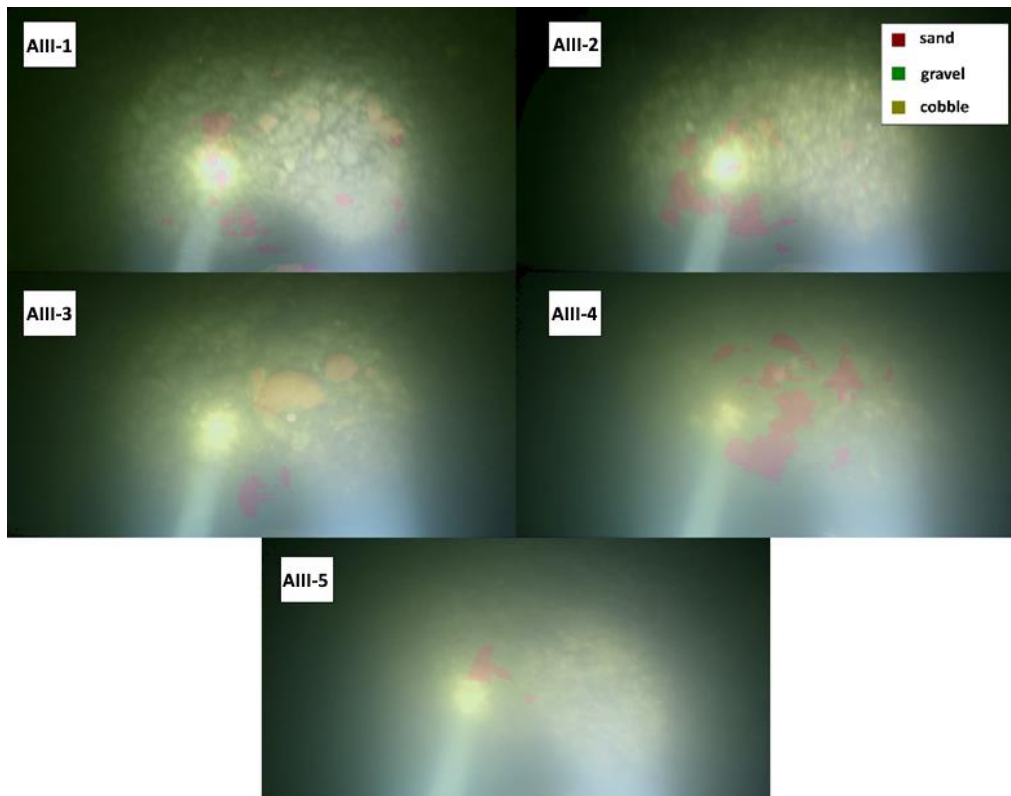
1119
1120 **Figure D5: Riverbed video images overlapped with their raw, DL detection result, at the sampling points in Section A**
1121 **- III.**
1122

1123   **Appendix E Site B – Section B - I**

1124
1125   **Figure E1: The path of the vessel and camera in Section B - I, Site B. The polyline is coloured based on the sediment**
1126   **seen during visual evaluation of the video. Yellow markers are the locations of physical bed material samplings. (Map**
1127   **created with Google Earth Pro)**
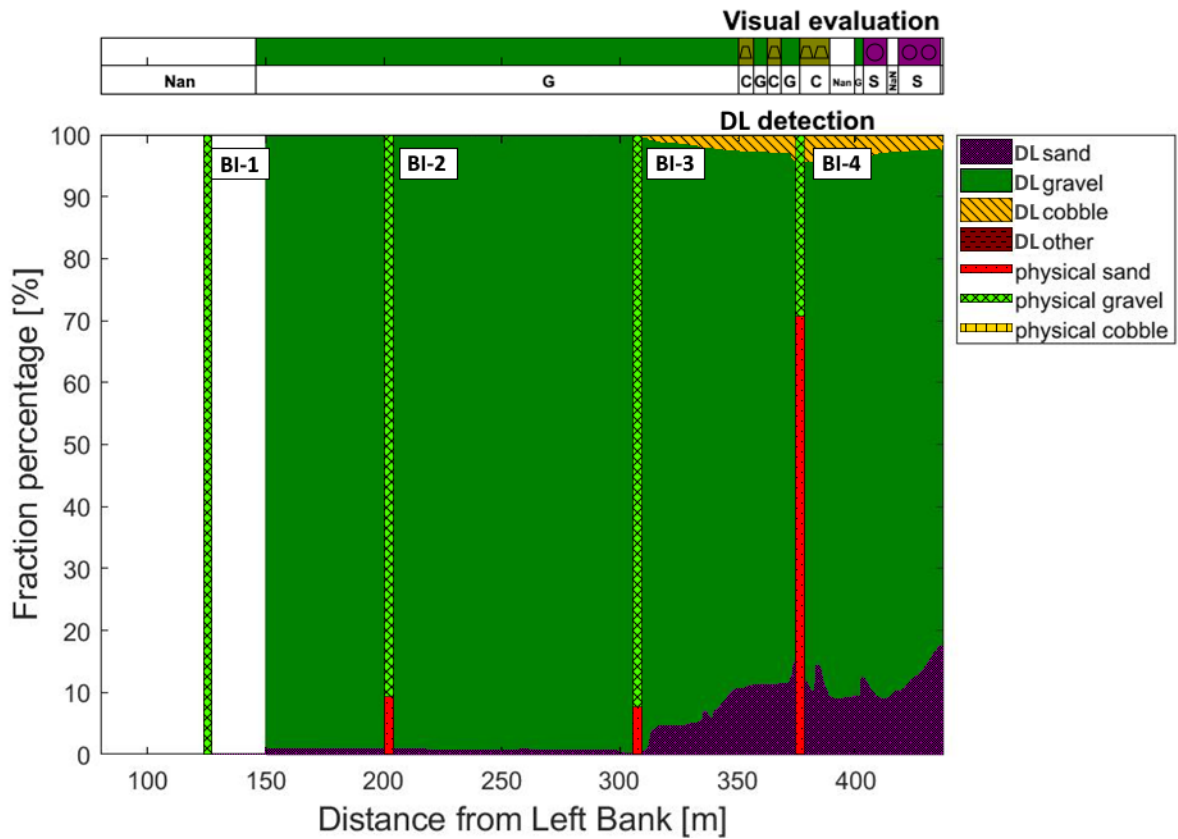
1128
1129   **Figure E2: Sediment fraction percentages in Section B - I, recognised by the AI. The visual evaluation included two**
1130   **classes: gravel – G, sand – S). The fractions of the physical samples are shown as verticals.**
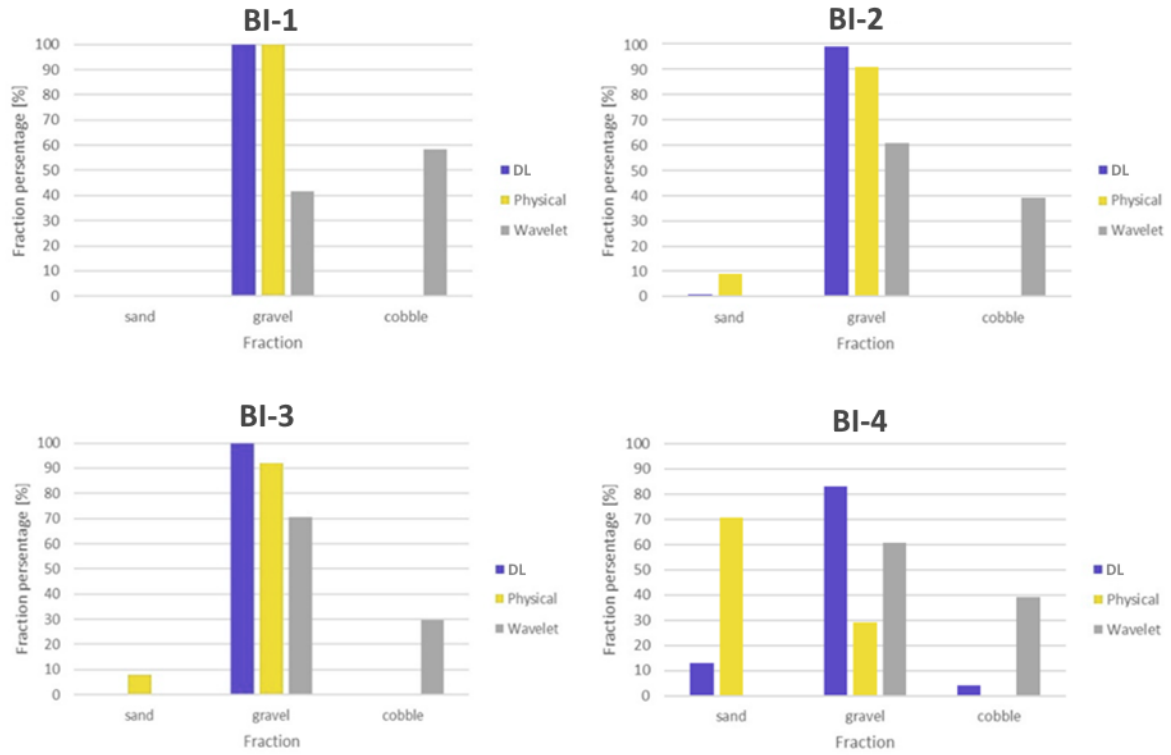
Figure E3: Comparison of sediment fraction % at the sampling locations from the moving-averaged DL detection, conventional sieving and the wavelet-based image processing method. Section B - I.
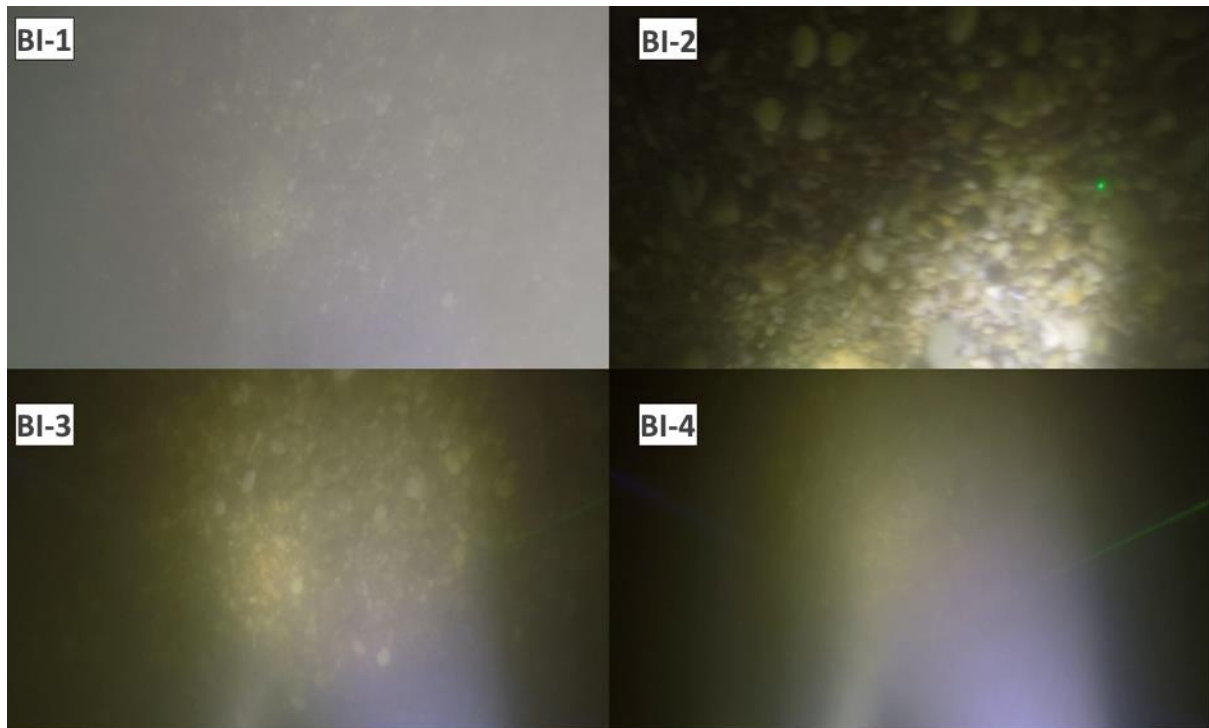
Figure E4: Riverbed video images at the sampling points in Section B - I.
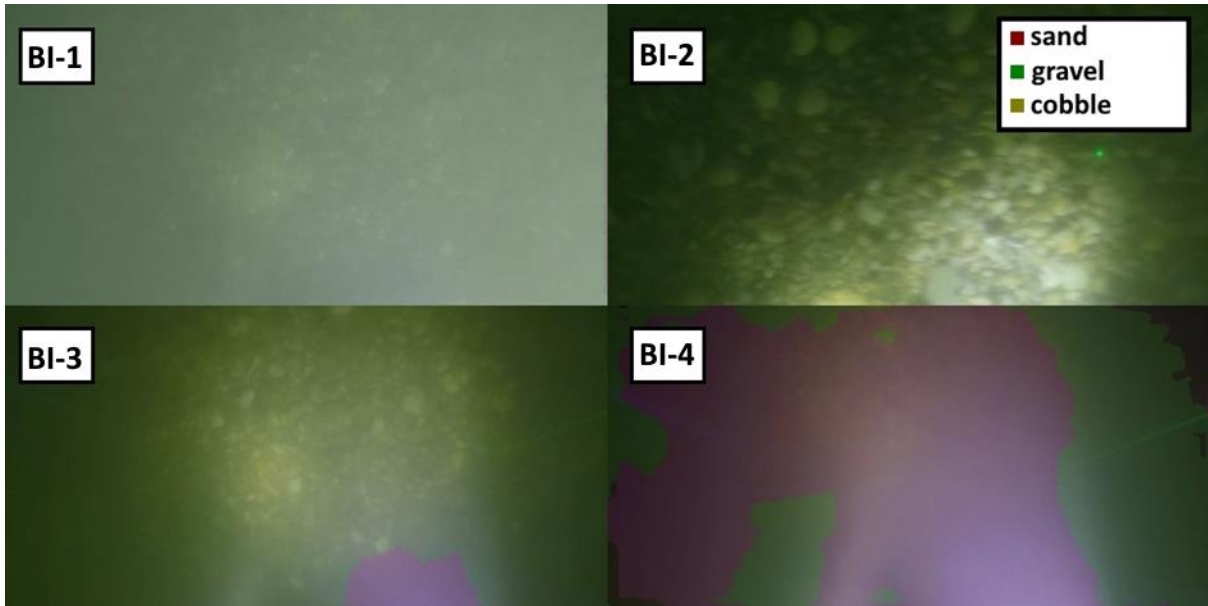
1137
1138 **Figure E5: Riverbed video images overlapped with their raw, DL detection result, at the sampling points in Section B**
1139 **- I.**

1140

1141 **Appendix F**
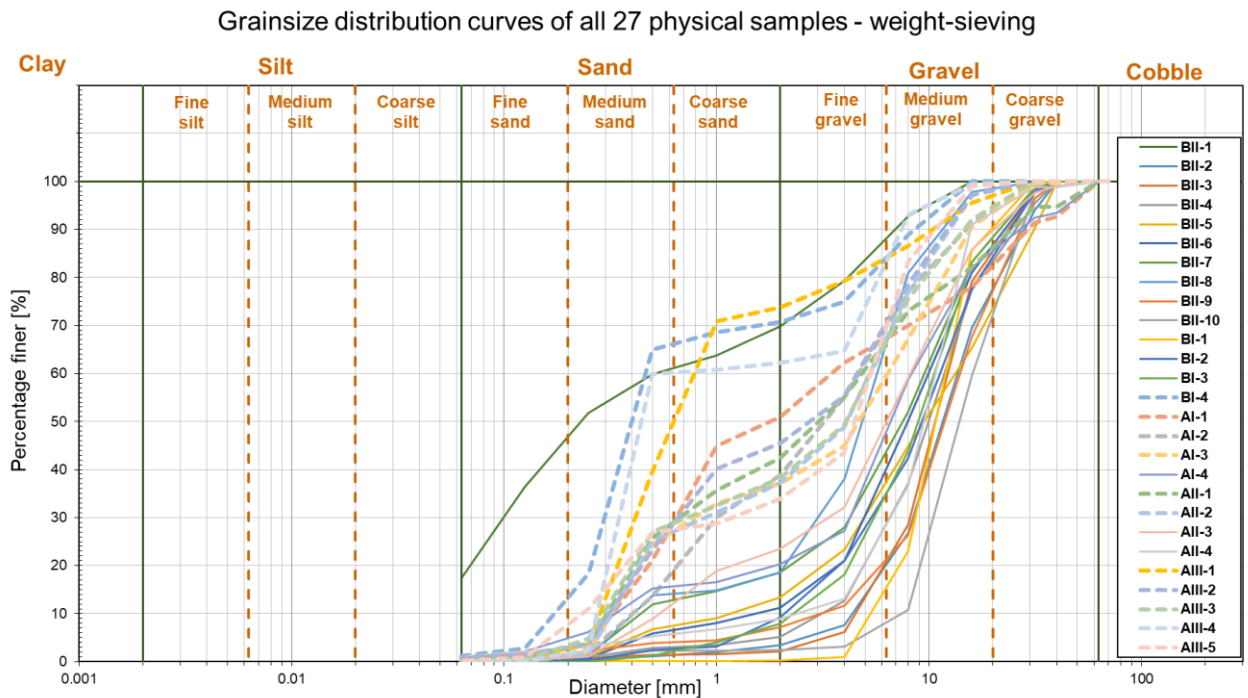
1142
1143 **Figure F1: Grainsize distribution curves of the 27 sieved physical samples. 11 curves categorised as Outlier Type-A are**
1144 **showcased with dashed lines. The shapes of these curves are representing bimodal (gap graded) sediment distributions,**
1145 **which typically refers to bed armouring (i.e., excess of a certain particle size, a coarser surface layer protects a finer**
1146 **subsurface layer from being washed away). Hence, analysing images of the surface layer could not represent these**
1147 **complex distributions inherently.**